Published in final edited form as:
Nature. 2018 June ; 558(7711): 564–568. doi:10.1038/s41586-018-0246-4.

Macromolecular organic compounds from the depths of Enceladus

Frank Postberg[#1,2], **Nozair Khawaja**[#1], **Bernd Abel**[3], **Gael Choblet**[4], **Christopher R. Glein**[5], **Murthy S. Gudipati**[6], **Bryana L. Henderson**[6], **Hsiang-Wen Hsu**[7], **Sascha Kempf**[7], **Fabian Klenner**[1], **Georg Moragas-Klostermeyer**[8], **Brian Magee**[5,7], **Lenz Nölle**[1], **Mark Perry**[9], **René Reviol**[1], **Jürgen Schmidt**[10], **Ralf Srama**[8], **Ferdinand Stolz**[3,11], **Gabriel Tobie**[4], **Mario Trieloff**[1,2], and **J. Hunter Waite**[5]

[1]Institut für Geowissenschaften, Universität Heidelberg, 69120 Heidelberg, Germany [2]Klaus-Tschira-Labor für Kosmochemie, Universität Heidelberg, 69120 Heidelberg, Germany [3]Leibniz-Institute für Oberflächenmodifizierung (IOM), Universität Leipzig, D-04318 Leipzig, Germany [4]Laboratoire de Planétologie et Géodynamique,UMR-CNRS 6112, Université de Nantes, France [5]Space Science and Engineering Division, Southwest Research Institute, San Antonio, TX 78238, USA [6]Jet Propulsion Laboratory, California Institute of Technology, Pasadena, CA 91109, USA [7]Laboratory for Atmospheric and Space Physics, University of Colorado, Boulder, Colorado 80303, USA [8]Institut für Raumfahrtsysteme, Universität Stuttgart, 70569 Stuttgart, Germany [9]Applied Physics Laboratory, Johns Hopkins University, Laurel, MD 20723, USA [10]Department of Physics, University of Oulu, 90014 Oulu, Finland [11]Wilhelm-Ostwald-Institut für Physikalische und Theoretische Chemie, Universität Leipzig, 04103 Leipzig, Germany

[#] These authors contributed equally to this work.

Abstract

Saturn's moon Enceladus harbours a global ocean[1], which lies under an ice crust and above a rocky core[2]. Through warm cracks in the crust[3] a cryo-volcanic plume ejects ice grains and vapour into space[4–7], providing access to materials originating from the ocean[8,9]. Hydrothermal activity is suspected to be occurring deep inside the water-percolated porous core[10–12], powered by tidal dissipation[13]. So far only simple organic compounds with molecular masses mostly below 50u have been observed in the plume[6,14,15]. Here we report observations of emitted ice grains

Correspondence and requests for materials should be addressed to F.P., Frank.Postberg@geow.uni-heidelberg.de.

Data availability statement:
All CDA data used for this analysis are archived on the Small Bodies Node of the Planetary Data System (PDS-SBN), at http://sbn.psi.edu/archive/cocda. The exact time stamp of each data is listed in Extended Data Table 1.

Author Contributions:
F.P. led the writing of the manuscript, N.K. and F.P. led the CDA data analysis with support from L.N., G.M.K. and R.S. designed the CDA observation, N.K., H-W.S., S.K., L.N., F.P. did the programming and CDA data reduction, F.K., R.R., F.S., M.S.G., B.L.H. conducted lab experiments, J.H.W. led the INMS observation, B.M. and M.P. conducted the INMS data reduction and analysis, F.P., J.S., C.R.G., M.T., G.T., G.C., M.S.G., B.A. are responsible for the geophysical and geochemical interpretation of the data. All authors contributed to the discussion and commented on the manuscript.

Author information:
The authors declare that there are no competing financial interests.

Europe PMC Funders Author Manuscripts

containing concentrated, complex, macromolecular organic material with molecular masses above 200u. The data provides key constraints on the macromolecular structure and is suggestive of a thin organic-rich film on top of the oceanic water table. There, organic nucleation cores generated by bubble bursting allow probing of Enceladus' organic inventory in drastically enhanced concentrations.

Two mass spectrometers aboard the Cassini spacecraft, the Cosmic Dust Analyzer (CDA) and the Ion and Neutral Mass Spectrometer (INMS), performed compositional in situ measurements of material emerging from the subsurface of Enceladus. These measurements were made inside both the plume and Saturn's E-ring which is formed by ice grains escaping Enceladus' gravity[16].

The CDA records time-of-flight (TOF) mass spectra of cations generated by high-velocity impacts of individual grains onto a rhodium target with a mass resolution of $m/\Delta m \approx 20–50$[14,17]. Previous CDA measurements showed that about 25% of E-ring ice grain spectra, so-called Type 2 spectra, exhibit organic material[8,9,14]. A subgroup (≈ 3%) of Type 2 spectra (Methods 1b,c, Extended Data (ED) Tab. 1) is characterized by a sequence of repetitive peaks beyond 80u usually separated by mass intervals of 12u to 13u in most cases (Fig. 1). This sequence in most cases extends up to the maximum mass nominally covered by CDA at about 200u. The broad and irregular shape of the peaks indicates that they are composed of multiple unresolved overlapping mass lines (Fig. 1a and ED Fig. 1). The mass intervals between the peaks suggest organic species with an increasing number of carbon atoms (C_7 – C_{15}), which we refer to as High Mass Organic Cations (HMOC). While an interval of 14u would indicate the addition of a saturated CH_2 group to an organic 'backbone', the actual average mass difference of 12.5u indicates the presence of predominately unsaturated carbon atoms.

In principle each HMOC peak could be derived from a different parent molecule. However, monotonic decrease without major intensity variations from 77u to 191u (Fig.1a, ED Fig. 1) rather indicate fragments from higher-mass parent molecules (outside the CDA's nominal mass range) and not a conglomerate of several molecules with masses below 200u. This interpretation is consistent with the observation that the detection probability increases with impact speed (Methods 1c, ED Tab. 1), increasing the available energy for fragmentation and ionization. A similar fragmentation pattern has been observed in impact experiments with polymers[18,19] containing aromatic subunits (ED Fig. 2, Methods 2).

In addition to the nominal mass spectrum (1u to ≈200u) CDA records extended TOF-spectra of the same individual grains up to about 8000u with resolution and sensitivity uniformly reduced by a factor of ten. These extended spectra exhibit abundant macromolecular cations with masses in excess of 200u in most HMOC-type spectra (ED Fig. 5). This further supports the interpretation that fragmentation of macromolecular parent molecules or networks creates the HMOC.

The HMOC sequence always appears together with intense non-water signatures below 80u (Fig. 1) offering further compositional and structural constraints. Although there is some variation (ED Figs. 1, 4) non-water peaks are arranged in 6 groups at 15u, 27 - 31u, 38 - 45u,

Europe PMC Funders Author Manuscripts

51 - 58u, 63 - 67u, and 77 - 79u and like the HMOC pattern indicate a sequence of organic species with increasing number of carbon atoms. Organic mass lines below 45u show up preferentially at uneven masses (Fig 1b) indicating a typical cationic hydrocarbon fragmentation fingerprint. However, from stoichiometry the mass lines at 30u, 31u 44u and 45u cannot be pure hydrocarbon cations and indicate O and/or N bearing cations from hydroxyl (CH_2OH^+, CH_3-CH-OH^+), ethoxy, or carbonyl functional groups and/or nitrogen-bearing ions (e.g., $CH_2NH_2^+$, CH_3-CH-NH_2^+), (Fig. 1b, ED Fig. 4).

A prominent peak preceding the HMOC sequence (Fig. 1b) indicates abundant cationic forms of a benzene ring, phenyl ($C_6H_5^+$, 77u) and benzenium ($C_6H_7^+$, 79u). The high abundance of these cations is highly diagnostic because the energetically favorable cationic aromatic structure would be tropylium cations[18,19,20] ($C_7H_7^+$, 91u). (Fig. 1a). Formation of tropylium cations must thus be inhibited requiring aromatic precursor molecules without hydrogenated C-atoms (e.g., alkyl groups) attached to the ring[20,21] (Fig. 2, ED Fig. 7, Methods 2).

A high abundance of aromatic structures is further supported by mass lines at 63u - 65u ($C_5H_{3,4,5}^+$), 51u – 53u ($C_4H_{3,4,5}^+$) and 39u (C_3H_3) (Fig. 1b, ED Fig. 1) that can be interpreted as coincident unsaturated benzene fragments[21] (Fig. 2, ED Fig. 7). However, also aliphatic fragmentation is indicated by strong peaks at 27u - 29u ($C_2H_{3,4,5}^+$), 41u – 43u ($C_3H_{5,6,7}^+$), and less pronounced at 15u (CH_3^+). Mass lines at 55u – 57u are in agreement with aliphatic C_4 species ($C_4H_{7,8,9}^+$), whereas aliphatic structures with more than 4 C atoms (e.g., $C_5H_{9,10,11}^+$ / 69 - 71u) are generally absent (Fig. 1).

Each spectrum also exhibits water cluster cations of the form $H_3O(H_2O)_n^+$ (Fig. 1), typical for water ice impacts[14,17]. Evidently, an ice/organic mixture constitutes the bulk composition of these particles. Ion abundances are indicative of an organic fraction in ice grains up to the percent level (ED Fig. 7). Particle radii are mostly between 0.2 and 2 μm (ED Tab. 1). Na^+ ions and sodium/water cluster ($Na(H_2O)_n^+$) appear in most HMOC spectra but at much lower level than in spectra of Type 3 grains, which are thought to be generated from frozen spray of Enceladus' salty ocean[8,9]. In HMOC-type spectra the Na/water ratio is similar to the low abundance found in Type 1 particles thought to condense from salt-poor water vapour[22,8].

Cassini's INMS has measured the integrated composition of the Enceladean plume at several flyby speeds[12]. In contrast to CDA, which records cations forming upon impact, INMS simultaneously measured the composition of neutral gas entering the instrument aperture and volatile neutral molecules that are generated upon ice grain impact onto the instrument's antechamber[23] (Methods 3). There is a striking overabundance of organic species in spectra obtained at high flyby speeds (14 – 18 km/s) compared to those obtained at slower velocities (7 – 8 km/s) that we attribute to fragmentation of large organic parent molecules beyond the upper INMS mass limit at 99u (Fig. 3). Given the low temperatures, species above 99u are expected to be extremely depleted in the plume gas and rather originate from ice grains, probably of HMOC-type, entering the INMS aperture at high speed.

Mass lines at 77 – 78u stand out in full agreement with the CDA inference of benzene species. Because these are only apparent at high flyby speed they cannot stem from benzene itself but, like the other species in the residual spectrum, must be fragments from larger parent molecules. As in the case of CDA, some of the smaller require oxygen-bearing fragments. Further INMS compositional analysis of signals extracted explicitly from ice grain impacts (ED Fig. 10, Methods 3b) provides further evidence that CO is the dominant fragment species at 28u and that an N-bearing fragment (C_2H_3N) might be present.

In spite of the relatively low mass range and resolution of the Cassini mass spectrometers, the measurements lead to the following key constraints: 1) The HMOC-pattern in CDA spectra and the extended spectra argue for the presence of organic molecules with masses clearly above 200u. 2) The typical spacing of 12u – 13u between HMOC peaks implies unsaturated cationic fragments with a ratio C/H ≈ 2. Impact experiments with polystyrene[18,19] (ED Fig. 2) indicate that the C/H ratio of the parent molecules might be lower (C/H ≈ 1) than in these fragments. 3) Prominent benzene-like species in CDA and INMS spectra indicate the presence of abundant sub-structures of isolated benzene rings. From INMS spectra the features cannot originate from benzene itself and are fragments of larger molecules. However, PAH-like fused rings do not form such fragments. Although not unique, the most parsimonious interpretation is that these aromatic structures are parts of the same massive parent molecules responsible for HMOC, which would explain their unsaturated nature. 4) From the suppressed formation of tropylium cations in CDA spectra we conclude that the rings are either connected to functional groups without C-atoms or to dehydrogenated C-atoms. 5) Unsaturated species at low masses are in close agreement with aromatic fragmentation. Aliphatic cations indicate saturated aliphatic structures with 1 to 4 C atoms in parallel to the unsaturated (aromatic) structures. 6) Oxygen-bearing species indicated in both CDA and INMS spectra likely originate from hydroxyl, ethoxy and/or carbonyl functional groups. Nitrogen-bearing species are in good agreement with some features but not a unique interpretation. No indication of other elements in the organic structures is observed, but these cannot be ruled out either.

Fragmentation of a single type of macromolecule may be responsible for all mass lines in HMOC spectra. The parent substance would then be composed of cross-linked or polymerized aromatic and aliphatic substructures with functional groups containing oxygen and likely nitrogen. Alternatively, contributions from lower mass species might be mixed with macromolecules.

An Enceladus origin of these macromolecules is evident (Methods 6, 7) and there is a multitude of speculative options for the genesis of these complex organics on Enceladus, some of which outlined in Methods 5. However, the data provides definite clues on the formation of the highly organic-enriched ice grains. Ice grains of very different salinity emerging from Enceladus have previously been identified in CDA mass spectra. Nearly pure water ice grains (Type 1) can form from condensation of supersaturated vapor inside and above the ice vents[8,22,24]. Salt rich ice grains (Type 3), however, are thought to be frozen ocean spray[8,9], generated when bubbles of volatile gas (CO_2 25, CH_4, or H_2 [12]) reach the water table and burst[26]. The HMOC-producing organic material (Methods 6), is detected in Type 2 salt poor ice grains and thus cannot have formed directly from the salty ocean spray

that preserves the liquid composition upon flash freezing[9]. Consequently, the observed organic compounds were not dissolved in ocean water when incorporated into ice grains. But molecules with masses much larger than 200u should not exist in the gas phase near the water table ($T \leq 0°C$) so that the organic substances cannot have condensed from the vapor either and instead must have been solid when the grains formed.

The most plausible way to generate the observed grains is if the organic material exists as a separate phase, such as a thin film or layer of mostly refractory, insoluble organic species on top of (at least parts of) the oceanic water table located inside water-filled cracks in the ice crust (ED Fig. 12, Methods 4). Bursting bubbles then disperse the organic film and, besides salty water droplets, produce droplets or flakes of organic material. Ascending in the icy vents the organics become coated by water ice condensing from the vapor carrying the grains (ED Fig. 12). Indeed, the limited tendency of benzene cations in HMOC spectra to cluster with neutral water molecules disfavors intimate mixing of organics with water and rather implies a core/shell grain structure. In a well-mixed system this cluster at 95u is much more pronounced (ED Fig. 7).

Aerosol formation from bubble bursting is a well-studied process in Earth's oceans, which are covered by an organic micro layer26. Organic-bearing sea spray serves as highly efficient nucleation cores of ice clouds over polar waters on Earth[27] and is found preferentially in the smallest aerosols between 40 nm and 250 nm in size[28,26], whereas larger aerosols with sizes between 500 nm and 1000 nm are either organics mixed with salt or are entirely without organics[29]. Under Enceladus' low gravity conditions one would expect larger gas bubbles and therefore somewhat larger film drops. Spectra showing HMOC are generated by ice grains with radii around 1μm (ED Table 1). Insoluble organic nucleation cores, a few hundred of nm in size, would naturally explain the high organic content in HMOC grains. Larger, organic-free salty ocean droplets account for the salt rich Type 3 particles detected by CDA. Bubbles ascend through tens of kilometers of ocean before reaching the surface. Like in Earth's oceans, organic substances can accumulate efficiently on the bubble walls[30] thus probing the oceanic organic inventory at depth (Methods 4).

Methods

1) CDA Data analysis

a) Short description of CDA's Chemical Analyser Subsystem—The Chemical Analyser (CA) is the subsystem of the Cosmic Dust Analyser[31] (CDA) that provides chemical information about an impacting dust particle. Depending on the trajectory of the particle, it either hits the central rhodium target (Chemical Analyser Target—CAT, diameter: 0.17 m), the surrounding gold target (IIT, diameter: 0.41 m), or the inner wall of the instrument. This work only deals with impacts on the CAT. If a dust particle impacts the CAT with sufficient energy the particle is totally vaporized and partly ionized, forming an impact plasma of target and particle ions, together with electrons and neutral molecules and atoms. The instrument separates this plasma, the positive component of which is linearly accelerated towards a multiplier about 19cm away, used to generate a time of flight (TOF) spectrum. The spectrometer is sensitive to positive ions only. The mass resolution ($m/\Delta m$),

derived from laboratory experiments with the instrument, depends on the atomic masses of the ions. At 1u, m/**Δ**m is 10, increasing to 30 m/**Δ**m at 100 u and up to 50 m/**Δ**m at 190 u, although these values strongly vary with impact conditions.

Acquisition of a spectrum in the high rate sampling mode of the multiplier can be triggered by charge thresholds being exceeded on either the CAT or the multiplier. In the latter case recording can be triggered up to several μs after the actual impact by the arrival of an abundant ion species, For water dominated particles these generally are hydrogen cations (H^+) or hydronium ions (H_3O^+). If triggered by the arrival of H_3O^+, mass lines of species with lower masses than 19 u, as well as the hydronium signature itself, do not appear in the spectrum. For this work all spectra were either triggered by impact or by registering the H^+ signal at the multiplier.

The spectra are logarithmically amplified, digitized at 8 bit resolution and sampled at 100 MHz for a period of 6.4 μs after the trigger. The recording period of the high-rate sampling mode allows the detection of ions with masses of up to approximately 185 u, assuming instrument recording is triggered by the impact itself and about 215 u when triggered by H^+. The extended spectrum starts after the high-sampling mode ends at 6.4 μs and is recorded with a sampling rate of 10 MHz up to a total time of 40 μs. The low number of data points corresponds to an extremely low mass resolution in the extended spectrum: one data point interval represents 7 u at 300 u and 20 u at 2000 u. The extended spectrum frequently shows an instrument-artefact-peak at 6.8 μs, which is ignored in our analysis.

Since the TOF is proportional to the square root of the mass to charge ratio of ions, its spectrum in an ideal case also represents a mass spectrum for identical ion-charges. The ions created by impact ionization in the impact speed regime considered here (4 – 18 km/s) are almost exclusively singly charged. Unfortunately, the TOF is also influenced by the broad distribution of initial ion velocities, slightly varying flight paths, and plasma shielding effects[32]. For that reason species with identical mass are distributed over a range of sampling points and the mass resolution drops below integer values usually around 25 - 30u. Therefore we prefer to display original CDA spectra with an x-axis showing time-of-flight and not mass. The latter could mislead the reader to intuitively assume an unrealistically high accuracy.

For a detailed description of the instrument see Srama et al. (2004)[31]. The calibration routine is described for example in Postberg et al. (2006, 2008)[33,14]. For the data set in this work the calibration was generally done by using water and sodium mass lines and a stretch factor of a = 474 ns was applied.

b) Data set—All data used for this work are listed in Extended Data Table 1 and, like all CDA data, is archived on the Small Bodies Node of the Planetary Data System (PDS-SBN), at http://sbn.psi.edu/archive/cocda. We used 15 periods covering good pointing of CDA towards the E ring dust RAM between 2004 and 2008. This early period was chosen because CDA contamination from salts deposited on CDA impact target during deep Enceladus plume dives is negligible[17]. In the following the periods are listed in second units using the Spacecraft Clock (SCLK):

Europe PMC Funders Author Manuscripts

- 1477548025 – 1477746968
- 1489004979 – 1489118561
- 1498469760 – 1498505448
- 1506223870 – 1506436625
- 1509311996 – 1509357627
- 1511686278 – 1512480582
- 1514090477 – 1514186815
- 1515560669 – 1516328727
- 1519522033 – 1519612908
- 1521596023 – 1522361262
- 1543798083 – 1543831204
- 1544838694 – 1544916311
- 1557517652 – 1557520425
- 1589065736 – 1589083623
- 1605559719 – 1605566052

Within these periods a total of 7353 spectra of impinging E ring grains were investigated. A Lee filter was applied for better signal to noise. Within the group of organic-bearing spectra (Type 2[14,8,9]) we find a subgroup of spectra with a pattern of repetitive non-water peaks above 80u (Fig. 1). We call the spectral pattern High Mass Organic Cations (HMOC). Selection criteria are the following

- at least 5 roughly well defined equidistant peaks above 80u with a signal to noise significance > 2σ.
- Water cluster peaks of the form $(H_2O)_n\ X^+$ with x being e.g. H_3O^+ or Rh^+ are explicitly not considered for selection. Cases where an HMOC a pattern could be verified despite interference with water clusters were selected but not considered for the sub-selection high quality spectra (see Methods 1d)
- Isolated or irregular peaks above > 80u are not considered.

Under the definition of CDA Type 2 grains[14] the multitude of all organic bearing ice grains observed in the plume and in the E ring is summarized. Spectra other than the specific Type 2 spectral subtype displaying HMOC are outside the scope of this work.

c) Relative frequency of HMOC-type grains depends on impact speed and distance to Enceladus orbit—We find 83 spectra (1.1 %) with apparent HMOC, equivalent to about 3 % of all Type 2 spectra in the dataset (ED Table 1). However, the probability of HMOC detection depends on the impact speed and thus the energy densities the organic bearing ice particles were exposed to upon impact. At high speeds (8 - 15 km/s) the overall frequency of HMOC detections is about 3 % of all particles (≈ 10% of Type 2).

At 6 to 8. km/s it drops sharply to about 1 % and goes down to 0.4 % between 5 and 6 km/s (see ED Table 1). Below 5 km/s no HMOC has been detected equivalent to a probability of < 0.1 %. Within the few spectra in the data set recorded at speeds above 15 km/s HMOC have not been detected (equivalent to a probability of < 1.7 %), so the speed range of 8 – 15 km/s seems to be optimal for CDA to record HMOC spectra. At speeds below 8 km/s the probability to produce fragments from the proposed parent molecules (outside the CDA mass range) decreases, and becomes close to zero below 5 km/s. At speeds above 15 km/s the detection probability seems to decrease again, probably due to the fact that at these high impact speeds mostly small fragments with masses < 80 u are produced, whereas fragments that yield the typical HMOC pattern between about 80 u and 200 u (the defining feature of this CDA spectrum type) become less likely.

HMOC grains have been detected in the plume (ED Fig. 6) and in the E ring at a wide range of Saturnian distances, from 3.8 to 14 R_S, except in its outermost fringe that extends out to 20 R_S [34]. However, the fraction of HMOC-type grains in the E ring increases closer to Enceladus orbit. The chance to encounter an HMOC grain with intermediate impact speed of 6 to 8 km/s is about 2.5 % at a Saturnian distance of 3.8 – 5 Rs, drops to 1.5% at 5 – 7 Rs. Outside 7 Rs the detection probability goes down sharply to 0.5% and is 0.3% beyond 11 Rs. This clearly points at an Enceladus origin (see Methods 6).

The effects of speed and distance are cumulative: in the optimal speed window and close to the orbit of Enceladus the detection rate is highest at about 4%. Thus we can conclude that the actual fraction of ice grains carrying substantial amounts of complex organic material ejected into the E ring is at least 4 % of grains in the size range covered by CDA ($r \approx 0.2 – 2\mu m$). An instrument with an extended mass range (e.g. up to 2000u) and higher resolving power than CDA would likely detect complex organics with similar or higher probability at encounter speeds of ≈ 5 km/s with the organic parent molecules being largely intact.

d) Selection of 64 “high quality” spectra out of 83 for Figure 1 and Extended Data Figures 1 and 3—For the peak statistics and co-added spectra in Fig. 1 and ED Fig. 3, and the semi-quantitative spectra depicted in ED Fig. 1 we used a subset of 64 spectra that had the highest quality. The 19 spectra that were not selected either had

- **i)** an extended water cluster pattern (e.g. $(H_2O)_n$-H_3O^+ or $(H_2O)_n$-Rh^+) where strong peaks overlapped into the HMOC region above 100 u.
- **ii)** a low signal to noise HMOC pattern with poor peak definition that did not allow for a reliable quantification of all features.
- **iii)** an irregular baseline (instrument artifact) that did not allow for a reliable quantification and would have spoiled the quality of co-added spectra.
- **iv)** an uncertain calibration, which does not allow a unambiguous assignment of peak masses.

In case of i) and ii) the organic fraction in the ice grains is probably somewhat lower than in other HMOC spectra.

For ED Fig. 3 the data set was split into “fast“ and “slow” impacts. The lower panel is composed from 12 of the 64 high quality HMOC spectra recorded after a fast impact (> ≈ 10 km/s). In this case the speed was determined by the presence of one or more hydrogen cations (H^+, H_2^+, H_3^+). The uncertainty of this method is clearly below the uncertainty from assumptions on the orbital elements shown in ED Tab. 1. The appearance of H^+ cations is a reliable indicator of impact speeds in access of about 12 km/s[17,35], H_2^+ and H_3^+ cations appear already at slightly lower speeds (> 10 km/s)[17]. For 12 spectra, where a respective mass line was present, this reliable speed threshold indicator was used; the remaining high quality spectra were co-added to produce the ‘slow’ spectrum in ED Fig. 3. Due to the higher kinetic energy upon impact, low-mass cationic fragmentation species are more abundant there. Moreover, “fast” spectra were on average triggered earlier, mostly directly after impact (see Methods 1a). Therefore, the high rate recording interval of 6.4μs stopped at a lower equivalent mass than for the slower speed spectra (ED Fig. 1), and the HMOC peak at ≈ 191 u was often not recorded for “fast” spectra.

2) Inferring the origin of HMOC peaks in CDA spectra

In the main text we present arguments that the HMOC pattern is indicative of highly unsaturated organic cations. A very similar pattern was also observed in CDA ground calibration experiments using a dust accelerator[36] producing impacts from μm-sized polystyrene (PS) beads (Goldsworthy et al. 2003[18], Figs. 10, 13 therein). A few years later the accelerator experiment was repeated with identical results using an advanced TOF dust analyser providing higher mass resolution[19] (ED Fig. 2). A similar, but not identical, unsaturated cationic fragmentation pattern was observed in TOF-SIMS experiments with PS[37]. There, the most plausible explanation for the fragmentation pattern and the ionic species is given in Table 2 [37]. Although the spacing of the HMOC pattern of 12.5 u seems to suggest a C/H ratio of 2 or even higher, all three PS experiments show that such an unsaturated cationic fragmentation pattern can also be achieved with parent molecules with a C/H ratio of only 1. These analogue experiments demonstrate that the C/H ratio of the cationic fragments could be different from the bulk material.

However, there is a noticeable difference between PS spectra and HMOC spectra: In inversion to HMOC spectra, tropylium ions (91 u) form abundantly in impact ionization PS spectra, whereas phenyl cations (77 u and 79 u) are relatively depleted. In Fig. 2 we demonstrate the reason: in the PS polymer alkyl groups are attached to each of the aromatic monomers, which allow an easy formation of tropylium ions at 91u (ED Fig. 2). This is also known from classical electron ionization mass spectrometry: Only if the formation of tropylium ions is sterically difficult or impossible abundant phenyl cations form[20,21]. This leads to our conclusion that for HMOC parent species single-ringed substructures are predominately attached to dehydrogenated carbon atoms or to functional groups without carbon.

In the dust accelerator experiments with polymers an HMOC like pattern was observed at impact speeds of 4 – 6.5 km/s[18,19]. Above this speed further fragmentation occurred. In contrast, CDA HMOC spectra are observed at impact speeds of about 5 – 15 km/s. The water ice matrix, the HMOC parent molecules are embedded in, might explain this

difference. It is well known from Matrix Assisted Laser Desorption/Ionization (MALDI) experiments that water very efficiently protects large organic molecules from fragmentation.

An alternative interpretation of the origin of HMOC might be very large PAHs. However, in our laser assisted analogue experiment with pyrene in a water matrix (ED Figs. 8, 9, Methods 8), we do not observe efficient fragmentation of the PAH. These findings generally agree with the common knowledge from electron ionization (70 eV) mass spectrometry of a wide range of PAHs. In contrast, Stephan et al. (2003)[38] demonstrates a pattern similar to the one observed with CDA above 100u with TOF-SIMS from a mixture of high mass PAHs. However, the applied energies were much higher (25 keV) and the PAHs were not embedded in a water matrix, which naturally protects organic molecules from breakup[39]. In any case, regardless of fragmentation at harsh ionization conditions, PAHs do not yield any monoaromatic peak: neither phenyl (77 u) nor tropylium (91) cations form[40]. So if PAHs play a role in the origin of HMOC, other parent molecules must be responsible for the strong mono-aromatic peak in CDA and INMS spectra.

In principle mono-aromatic cations in CDA spectra (77 u, 79 u) could originate from benzene mixed within the macromolecules structure responsible for the HMOC. However, this is not possible for the benzene feature (78 u) seen in INMS spectra because there they exclusively appear at high-speed flybys and thus must be fragments of larger molecules. It is plausible to assume that the mono-aromatic features observed in both instruments originate from HMOC type ice grains (Methods 3) and therefore also in CDA spectra we consider molecular fragmentation as the most likely source.

3) INMS data analysis

a) Residual spectrum from ‘fast’ versus ‘slow’ flybys—The INMS[41] measurement routinely integrates the composition of plume gas over the flyby to increase signal to noise. Using this methodology, volatile compounds released from ice grains that fragment and evaporate upon impact onto the instruments antechamber[23] cannot be discriminated. In contrast to the CDA, which records cations, the INMS observes volatile neutral molecules that are in the vapor phase or generated by ice grain impacts in the plume and subsequently ionized by electron impact from 70 eV electrons in the ion source.

The residual spectrum presented in Fig. 3 represents the difference in composition and overabundance of organic material observed by the INMS during high velocity flybys when compared to low velocity flybys through the Enceladus plume (ED Fig. 11). Our interpretation is that low speed flybys result in minimal fragmentation of the organic compounds within the ice grains. In contrast high-speed impacts lead to fragmentation of large organic parent molecules beyond the INMS mass range of 99 u. Species with molecular masses above 99 u in the plume are expected to be extremely depleted in the gas phase and have to reside in or on ice grains. Based on the knowledge of the compositionally different ice grain populations CDA collected over many years, HMOC-type grains entering the INMS’s aperture are the most plausible source. Similarity in the composition of the fragments seen by CDA and INMS reinforce this assertion.

To obtain the spectrum shown in Fig. 3 we have taken the summed spectrum of the E5 flyby[15] and subtracted the average summed spectrum of the E14, E17, and E18 flybys. These represent the fastest (E5 at ~18 km/s) and slowest (E14/E17/E18 at ~8 km/s) flybys through the plume for which the INMS has the best data. The three slow flybys have been combined into an average spectrum to compensate for their lower signal-to-noise. Velocity-driven processes complicate the spectral comparison. H_2O -Ti reactions in the INMS antechamber increase with velocity due to vaporization of Ti from the walls of the instrument's antechamber and create excess H_2 from H_2O and leaving TiO and TiO2 as by products[15]. Likewise CO_2 more readily fragments to become CO as the velocity increases. Lastly, fragmentation products of high mass organics likely augment the plume gas signal of all masses dominated by organics in the INMS mass range. This makes it difficult to set an accurate reference point by which to compare the high and low velocity spectra. We have chosen to use the signal at 15 u of both spectra as the common reference point because the CH_3^+ dissociative ion from CH_4 dominates the signal at this mass, and CH_4 is considered to be a plume-derived volatile specie not significantly altered by fragmentation of high mass organics. Choosing mass 15u as the common reference point removes all signal in this mass for the spectra resulting from the subtraction, whereas signal in all other masses will be positive or negative. After matching the two spectra at their 15 u signal (ED Figure 11) and subtracting the low velocity spectrum from the high velocity spectrum, we then set the amplitude scale of the residual relative to the noise floor of the low velocity flybys (~5 orders of magnitude lower than the H_2O signal at 18 u) so that only significant residual signal is visible. The residual signal presented in Fig. 3 can be considered to be a conservative estimate of the high mass organic fragmentation effect – in case that the CH_4 for the high velocity flyby is increased from the low velocity flybys, the residual signal would be even larger in amplitude.

Hydrocarbon species in this conservative estimate of the residual signal are discussed in the main text. Moreover, it suggests that at least 50% of the 28u peak is from CO, given the upper limits placed upon N_2 and C_2H_4 in the 'fast' E5 spectrum[15]. The oxygen-bearing species H_2CO and CH_3OH are suggested as likely sources of the residual signal at 30u and 31u because they are the dominant species for these peaks in the E5 spectrum[15] and the residual retains more than 60 % of the original E5 signal. This interpretation is strongly supported by the INMS 'ice grain spectrum' (Methods 3b).

b) INMS 'spectrum of ice grains'—To isolate spectral signals from icy grains when crossing the plume we extracted those parts of the high time resolution real time INMS plume spectra (every 2.3 s) that registers the ice grains as spikes in the Closed Source Neutral (CSN) data[23,42]. The quadrupole mass analyser has a mass step Integration Period (IP) of 34 milliseconds, whereas the vaporized gas from the impact dissipates in the antechamber in less than 3 milliseconds. Therefore, the ice impacts appear as gas bursts or "spikes" superimposed on the smoothly varying gas spectra that are mass filtered by the mass step the analyser is presently dwelling on. Thus each spike can register only one unity mass location per ice impact. By summing the spikes over three similar encounters (E14, E17, and E18) there are sufficient mass sampling statistics over the full sampled mass range

to construct a pseudo mass spectrum that represents the composition of the micron-sized grains.

ED Fig. 10 shows the pseudo mass spectrum of the grains measured by INMS within 100 s of the time of closest approach. Each of the three encounters provided approximately 200 individual measurements or spikes to the composite spectrum. The vertical axis represents the relative count rate for each mass, as the counts for each mass are adjusted for the number of measurement opportunities (Integration Periods or IPs) for each mass. The scale of the plot is adjusted so that the minimum count rate is 1 count per IP. The dispersion in measurements from the three encounters represents the uncertainty in the count rates. The grain measurements are heavily concentrated near closest approach, peaking with more than one per every ten IPs at 2 u, which is the mass most sensitive to the grains. Analysis of the ice grain spectrum reveals a composition related to, but distinct from, the plume gas.

Two observations are particularly relevant to the high mass organic material presented in this work (ED Fig. 10). First is the clear dominance of CO at 28 u and lack of N_2. Applying the well-known dissociation from impact of 70 eV electrons in the INMS ionization chamber, CO_2 accounts for ≈ 3% of the 28u signal. N_2 has an upper limit of ~10% of the 28u signal due to the low signal at 14 u (N^+ dissociative ion) and may not be present at all. If present, C_2H_4 is limited to less than ≈ 6% of the 28 u signal. This leaves a requirement for CO as the dominant species at 28 u, which matches well the signal at 12 u and 14 u (C^+ and CO^{++} dissociative peaks). Although not a unique source, CO may be released from carbonyls in HMOC parent compounds by decarbonylation reactions during high-speed impacts of ice grains in INMS. The caveat here is that the INMS does integrate over all ice grains detected in the plume. Therefore CO from carbonates and/or bicarbonates found in Type 3 grains[9,11] might contribute here as well. The second observation is the likely presence of C_2H_3N. The signal pattern of 39-42 u suggests a species with its highest signal peak at 41 u and lower signal in the surrounding masses. C_2H_3N is the best candidate as it matches this 'stairstep' pattern extremely well. C_2H_3N also appears to be present in the plume gas spectra, possibly due to contamination from a distribution of small grains indistinguishable from the incoming gas.

Note that in contrast to the spectrum in Fig 3., these ice grain spectra were recorded at slow flyby speeds and show no significant signal above 50 u. Unfortunately ice grain spikes at the high velocity flyby (E5) are not abundant enough to compose a similar spectrum as shown in ED Fig. 10.

4) Deduction of an organic enriched layer at the Enceladean water table

The observation of high concentrations of solid material, found in a water ice matrix that does not represent the ocean's salinity but is emitted from a saline ocean source, requires specific conditions on the formation of these grains. Because of the low temperatures near the water table where the ocean water is in contact with the ice crust, we conclude that the HMOC parent species are solid. The fact that the organics are embedded in a salt poor water ice matrix indicates that they mostly are poorly soluble in water. In principle, primordial refractory organic substances trapped in the ice crust near the cracks, which become mobilized by the ascending vapor, could serve as an organic source. However, we disfavor

this scenario because the crack walls are continuously coated by fresh ice condensing from the vapor flow[43,44].

We rather promote a scenario, well known from ice cloud formation over polar waters on Earth[27]. There, organic aerosols of mostly biogenic origin[26] thrown up by bubble bursting serve as highly efficient nucleation seeds. When bubbles burst on Earth's ocean an organic-free sea spray forms in parallel with pure organic aerosols and mixed phase organic-bearing sea spray[29,45]. The organic mass fraction of sea-spray aerosol has been consistently shown to be inversely related to aerosol size[29,46,47] and is mostly water-insoluble[47,26]. The purely organic endmembers are found preferentially in the smallest aerosols[26,28] and, as shown in the main text, the size of the organic nucleation cores in oceanic sea-spray matches the CDA observation of organic concentrations up to the percent level quite well.

Aerosol formation on Earth also provides a plausible analog mechanism for the simultaneous production of salty ocean spray and organic aerosols: If the droplets are smaller than a few micrometers they can be thermally supported in the water vapor with gas densities slightly below the triple point against Enceladus' gravity. They don't fall back to the liquid, but are carried upwards through the ice vents by gas from evaporating water following the pressure gradient into space. In parallel to the formation of smaller organic aerosols, larger salty ocean droplets form, later detected by CDA as salt rich Type 3 particles in the plume and in the E-ring. The analog from Earth would also predict some larger mixed phase particles that carry both ocean salts and complex organics but these have not been identified by CDA. One explanation could be that the macromolecular HMOC parent substance might be hydrophobic and in that way, would naturally avoid forming mixed phase organic/sea-water aerosols.

On Earth bubbles are generated mostly by breaking of waves[27]. On Enceladus several volatile gases have been detected in substantial concentrations in the plume (CO_2, CH_4, NH_3 and H_2)[12] that will inevitably create bubbles when rising though the ocean, which then burst at the water table. In Earth's oceans, bubbles not only produce an aerosol, but are also very efficient in 'harvesting' organic molecules from the deeper oceanic environment by collecting these substances on their surfaces while ascending. The increase of relative organic concentrations observed near the surface of Earth's oceans by 2 to 3 orders of magnitude[48,49,50] suggests a selective transport of organic matter from the bulk seawater to the water table and then from the microlayer to atmospheric aerosols[51,29,27].

5) Possible precursor scenarios for the observed complex organics

There are many ways to explain the presence of complex organic materials in an icy moon in the outer solar system. The two general categories of origin are accretion of primordial material and endogenic synthesis. In the former hypothesis, the organic carbon on Enceladus would predate the formation of the moon, and Enceladus would have acquired an organic inventory via its building blocks (icy planetesimals). The latter hypothesis would employ hydrothermal systems inside Enceladus's porous rocky core[13] to produce complex organic molecules from small molecule precursors. This category of hypothesis can be broken down into several sub-categories characterized by molecular precursors. Organic compounds can be synthesized from more oxidized forms of carbon such as CO_2, CO, or formate[52,53]. More

reduced simple organic species (formaldehyde, methanol, and HCN) can also serve as feedstock for the synthesis of more complex organic compounds[54,55]. Methane is a relatively inert species, so it may be a less favorable carbon source, unless prolonged metamorphism or radiation chemistry is involved. Both abiotic and biotic processing of these precursors is possible. A mixture of spatially distinct (e.g., ocean vs. rocky core) sources is also not to be excluded at the present state of knowledge.

As an example of endogenic synthesis, relatively oxidizing hydrothermal conditions may promote the conversion of simple primordial organics into reactive unsaturated compounds, such as quinones, (poly)phenols, or aldehydes, which may polymerize in turn (possibly in the presence of catalytic minerals) to form relatively hydrogen-poor macromolecules. Macromolecules at Enceladus containing aromatic units with connecting short aliphatic chains that include more or less oxidized functional groups may resemble some humic substances on Earth. On Earth several pathways exist for the formation of humic substances during the decay of biogenic complex organic matter[56]. However, these macromolecules may also be formed via synthetic routes such as radical polymerization of phenolic compounds in the laboratory. Hänninen et al. (1987) [57] showed that humic acid-like polymers can be synthesized from homogeneous, well-defined starting materials under oxidative conditions. The polymers display clear signatures of phenolic, aromatic (olefinic), and carboxyl carbons, and the carboxyl carbons are present regardless of whether the monomeric unit possesses a free carboxyl group or not. Based upon this fact, it was concluded that a partial de-aromatization occurs during the oxidative polymerization of o- and p-diphenolic compounds. Hänninen et al. (1987) [57] also reported that the ^{13}C-NMR spectra and other features of the synthesized polymers resemble to a large extent the spectra of humic acids. The characteristics of these macromolecules are consistent with our observations derived from HMOC spectra.

One can also consider a primordial origin of organic materials, which would be the simplest possibility. If the rocky materials that were accreted by Enceladus were analogous to CI/CM/CR chondrites or refractory cometary solids, then a substantial organic inventory is inescapable. CI chondrites in particular contain ~2 wt. % insoluble organic carbon[58]. This insoluble organic matter (IOM) [59,60,61,62,63] is considered partly of primordial origin, i.e. inherited from the interstellar medium, and partly modified due to early hydrothermal processing on carbonaceous chondrite parent bodies. These asteroidal small bodies/ planetesimals accreted within a few Myr after solar system formation, heated up as a result of radioactive decay – mainly from ^{26}Al – and persisted at elevated temperatures causing hydrothermal alteration and metamorphism for at least a few tens of Myr after solar system formation. While analytical data for comets are much more limited, recent results from comet 67P indicate a much higher organic carbon content of ~30 wt. % in dust particles[64,65]. To put these extraterrestrial numbers into perspective, consider that hydrocarbon source rocks on Earth have an average total organic carbon value of ~2 wt. % [66].

It may be the case that Enceladus's organic matter is similar to chondritic IOM. The latter shows some compositional variability: Particularly in classes like CV and CO that experienced strong thermal metamorphism at temperatures of about 400°C-600 °C, both H/C and O/C ratios are lower (down to 0.1 and 0.05, respectively), while in more primitive

classes (CI, CM, CR) mild aqueous activity (100-200°C) prevailed and allowed the preservation of O/C ratios as high as 0.23, and H/C ratios of 0.8 [59]. IOM in CI, CM, and CR classes is considered to be the most primitive IOM type, and has an average composition of $C_{100}H_{70}O_{22}N_3S_7$. It is macromolecular, and most of the carbon is incorporated in small aromatic structures, with about 20 to 30 % of the carbon constituting aliphatic bonds. The maximum length is 7 carbon atoms for aliphatic bridges between aromatic units, and 4 carbon atoms for the side chains with a free end [60,61]. Functional groups containing O, N, and S are also abundant (see figure 2 in Remusat, 2014 [61]). These characteristics are consistent with our observations derived from HMOC spectra.

Because this subtype of IOM is thought to be product of mild thermal and aqueous alteration it is impossible to say based on present information if this alteration already happened inside icy planetesimals under the influence of ^{26}Al heating or only later on Enceladus. There, under the influence of tens of millions of years of hydrothermal processing[13], more primitive primordial organics could have been transformed into a different organic mixture.

In the following, we will briefly elaborate further on scenarios that invoke some level of processing of primitive organics on Enceladus. At a depth of about 60 km below the surface the ocean comes in contact with Enceladus' core. The cores very low density (≈ 2500 kg/m^3) suggests ≈ 20% porosity[2,13]. Due to the low pressures and modest temperatures in Enceladus' interior, an unconsolidated core with such porosities can be inherited from the accretion and differentiation process. Tidal forces will help to maintain this fragmented state so that ocean water can percolate through it, up to the present-day. There, temperatures around 100 °C (higher and increasing towards the core center) can be maintained over at least tens of millions of years. Depending on the permeability of the core, the entire ocean could be processed at temperatures higher than approx. 100°C within 25 - 250 Myr[13].

While primordial oxygenated and nitrogenous species such as alcohols, carboxylic acids, amines, and nitriles may be more soluble in liquid water and can be leached into the subsurface ocean of Enceladus, larger polymeric organics would exist as a separate organic layer. If not heated above ~300°C, these organics might remain largely unaltered over geological time scales. Intense interaction with water however might have oxygenated the macromolecules on one end to form micellar structures (hydrophilic exterior and hydrophobic interior), and preserved their structural integrity over the lifetime of Enceladus.

Alternatively, a large accreted inventory of IOM-like material could establish the potential for rocks in Enceladus's core to serve as the basis of a more evolved organic factory, similar to oil and gas generating sedimentary basins on Earth. To make this factory operational and enable consistency with the plume organic observations, organic compounds must be mobilized from source rocks. Hydrothermal activity[10,12] could facilitate this process. Cooking organic matter (metagenesis) in the core would crack it into smaller constituents, which may then be transported by fluid flow[13] as dissolved species, liquid droplets, or entrained particulates (of particular relevance to the observations). A possible Earth analogue for this general scenario is Guaymas Basin in the Gulf of California[67]. This type of scenario has also been suggested for the interior of Pluto[68].

Is a scenario of processing primordial organic materials in Enceladus's core consistent with the chemical and structural features of compounds detected in the plume? Before proceeding, it is important to emphasize that it is still an open question whether we are seeing features that are representative of bulk organic materials in the subsurface. Processes that could fractionate organic compounds from their hypothesized source region to our instruments include expulsion from the core, (bio)degradation, hydrophobic phase separation in the ocean, plume outgassing, and impacts during high-speed flybys. In light of these considerations, it seems prudent to focus on broad characteristics.

Our data show the presence of unsaturated carbon and the benzene ring in particular. The former finding accords qualitatively with elevated temperatures that promote entropically-driven (more product than reactant molecules) dehydrogenation reactions. Countering this effect might be high concentrations of H_2 in hydrothermal fluids[12]; however, hydropyrolysis experiments demonstrate that aromatic carbon can coexist with abundant H_2 [69]. The outcome on Enceladus presumably depends on the conditions of temperature and H_2 concentration, as well as the duration of heating and the availability of hydrogenation catalysts such as nickel metal. If primitive organic matter in chondrites[58] and comets[70] can serve as a guide, it can be expected that Enceladus would have accreted organic materials containing benzene rings. From the perspective of a primordial origin, it therefore makes sense to find the benzene ring as part of the organic structures at Enceladus. It is unknown how much thermal maturation has occurred, but complete graphitization can be ruled out as the presence of organic-bound hydrogen is implied by the data. This imposes a limit on the thermal history of the organic source rocks, which seems consistent with the persistence of a low-density core rich in hydrated silicates[2]. These organics have not been overcooked.

Two other compositional features are relevant to a general discussion. First, the likely presence of oxygen- and nitrogen-bearing functional groups is consistent with inheritance of these heteroatoms in accreted organic matter (O/C ≈ 0.2, N/C ≈ 0.04) [58,70] or their subsequent incorporation into organic structures by hydration or amination reactions (e.g., of C=C or C≡C) on Enceladus. The latter processes would be facilitated by the availability of liquid water and ammonia in the interior[12]. Having heteroatoms also constrains the degree of thermal maturation. The second feature that we wish to highlight is the presence of methane in the plume[12]. It must be cautioned that there are multiple ways to explain the origin of methane[71], but it is appealing to envision a common mechanism for the formation of the full spectrum of organic compounds found at Enceladus. The analogy to petroleum geochemistry on Earth implies that thermal processing of organic materials will inevitably produce some CH_4 accompanying more complex organics[66]. The exact quantity of thermal gas will depend on the nature of the organic source material and the environmental (e.g., redox) conditions. At Guaymas Basin, hydrothermal fluids have very high concentrations of CH_4 (~60 mmol/kg) [72]. If the rocky core of Enceladus is also organic-rich and heated sufficiently, then this becomes a plausible scenario.

Europe PMC Funders Author Manuscripts

6) Enceladus as the origin of HMOC parent molecules and exclusion of other potential sources

a) Photolysis in the E-ring—Most individual ice grains reside in the E-ring for months to a few decades before they collide (either with a moon or the main rings) or before they are completely eroded by plasma sputtering. The oldest populations are generally located further away from their origin, Enceladus, in the outer E ring[73,74]. In principle one has to consider the possibility that HMOC parent molecules are not from Enceladus but evolved by photolysis from originally simple organics to the observed complex compounds in the E ring or, alternatively, that the complex organics are from Enceladus but have been severely altered e.g. by dehydrogenation. However, several observations are not in agreement with these scenarios.

- CDA does observe the largest proportion of HMOC type ice grains in the (young) inner E ring as compared to the (old) inner E ring (Methods 1c). This argues for degradation of the observed complex organics with time in the E ring rather than their generation.
- During Cassini's E17 flyby one freshly ejected HMOC type ice grain was observed inside the plume (not part of the compositional analysis of this paper but shown in ED Fig. 6). Furthermore, CDA observes many HMOC at the locations close to Enceladus' orbit, where most grains have been ejected from the plume only a few days to few months ago.
- The INMS observations were directly made in the plume with freshly ejected material.

b) Instrument contamination—An intrinsic instrument contamination as a source for the abundant organics in the spectra can be excluded[17]. Another concern is the large polycyclic aromatic hydrocarbons (PAHs) in Titan's atmosphere, which may have deposited onto the surface of CDA's impact target during close Titan flybys. Several lines of evidence argue against a cross contamination from Titan:

- The first of HMOC spectra were already detected in 2004 and early 2005, before Cassini's first close flyby of Titan.
- CDA has a decontamination device that was used in between Titan flybys, which heats the CDA impact target to 100°C for several hours.
- No build up of organics in spectra of E ring grains over time can be observed.
- The fact that only about 1% of the E ring impacts show such a massive organic signature is not in agreement with a coating of organic contamination on the impact target.
- The trend to observe HMOC-type grains at a higher frequency closer to Enceladus orbit compared to the outer E ring (Methods 1c) is not in agreement with a contamination origin.

Europe PMC Funders Author Manuscripts

- Thousands of spectra from impacts of dust populations outside the E-ring (Stream particles & exogenous dust & main ring dust) never show HMOC features.

7) Contamination of INMS spectra from previous measurements is unlikely

The multiple environments encountered by INMS require an evaluation of the potential for one environment to deposit refractory material onto the surfaces of the CSN antechamber, and for that material to be released and measured at a later encounter. Of particular concern are the large polycyclic aromatic hydrocarbons (PAHs) in Titan's atmosphere and Enceladus' ubiquitous nanograins, which may fragment material deposited onto the antechamber surfaces, sputter the organic products, and thus release volatiles into INMS.

The strongest evidence that high-speed nanoparticles do not create false signals in the INMS spectra is that the amounts of PAHs encountered at Titan are insufficient to produce the INMS measurements during encounters such as E5. At Titan, both INMS and CAPS measure PAHs or their fragments, with benzene observed by both instruments. Waite et al.[75] and Lavvas et al. [76] analyzed these measurements to estimate the abundance of PAHs as functions of altitude and of mass. Combining these estimates with the conservative assumptions that every PAH molecule that enters the INMS CSN aperture during the Titan encounters is then released during E5, the resulting signal would be more than an order of magnitude below the level measured by INMS at the fast Enceladus flyby (E5) as detailed in the following paragraph.

Benzene density in Titan's atmosphere is well modeled by an exponential with a scale height of 15 to 20 km and a density of approximately $1x10^5$ molecules/cm^3 at 950 km [75]. Before E5, there were thirteen Titan encounters with INMS pointed to accept atmospheric neutrals, and approximately $1x10^{11}$ higher-mass molecules entered<y the INMS CSN antechamber during those encounters. To produce the E5 measurements, the CSN antechamber maintained a density of < $1x10^7$ molecules/cm^3 for at least 40 seconds for the heavier species. With a residence time of only a few milliseconds, >$1x10^{12}$ heavy molecules were required in the CSN antechamber during E5. The number of molecules encountered at Titan is thus at least a factor of ten below the number of molecules required in the CSN antechamber to produce the higher-mass count rates observed during E5.

There is further evidence that the INMS spectra are unaffected by previous encounters: The CSN spectra at Enceladus do not change over many years, despite scores of Titan encounters during that period. Nor is there any apparent dependency of the Enceladus spectrum on whether a Titan encounter occurred between sequential Enceladus flybys.

8) Description of the laser dispersion analogue experiments for icy dust impacts in Heidelberg

ED Fig. 9 shows a sketch of the experimental setup. A liquid water beam, in which the tested substances are dissolved, is injected into a high vacuum (5×10^{-5} mbar) through a quartz nozzle (opening radius 6 μm – 8 μm). The quartz nozzle is mounted on a 3 axis-manipulator. A HPLC pump (model 300c, Gynkotek) is employed to keep the flow rate constant at 0.17 mL/min. The liquid beam flow is stable for ≈ 3 mm downward and then

disintegrates into droplets. In order to maintain the high vacuum, the liquid pours into two liquid nitrogen cooled cryotraps. For performing the measurements, the water beam is hit by a pulsed infrared laser (Opolette HE 2731, OPOTEK; 20 Hz, 7ns pulse length), which operates at a wavelength of approx. 2850 nm and a pulse energy up to 4 mJ. The laser is directed and focused onto the liquid by three CaF_2 lenses and a gold mirror. The wavelength is chosen to specifically excite the OH-stretch of the water molecules. When the laser energy is absorbed by the water beam, the water is rapidly heated up and explosively disperses into fragments. In this way cations, anions, electrons and neutral molecules are created [39,77].

Depending on the operation mode, cations or anions, which pass through a skimmer, are analyzed in a reflectron Time of Flight mass spectrometer (Kaesdorf). This mass spectrometer is operating according to the principle of delayed extraction. The delaytime is adjusted with the aid of a pulse generator (model DG535, Stanford Research Systems). By adjusting the delaytime, ions with a distinct initial velocity are selected for detection at the Micro Channel Plate (MCP). In combination with different delaytimes, variable laser intensities are used to simulate different impact velocities of ice grains onto the Cosmic Dust Analyzer's target[78]. The detected signals are intensified by a preamplifier, visualized by a 12 bit digitizer card (Acqiris) and recorded using LabVIEW. Flow injection of the tested solutions is accomplished with an injection valve (model MX9925, Rheodyne). 500 single spectra are averaged to achieve the co-added spectra as presented in the Extended Data. The chemicals (p.A.) are purchased from Sigma Aldrich. All solutions are freshly prepared with doubly distilled H_2O in lockable 50 mL sample cups.

Europe PMC Funders Author Manuscripts

Extended Data

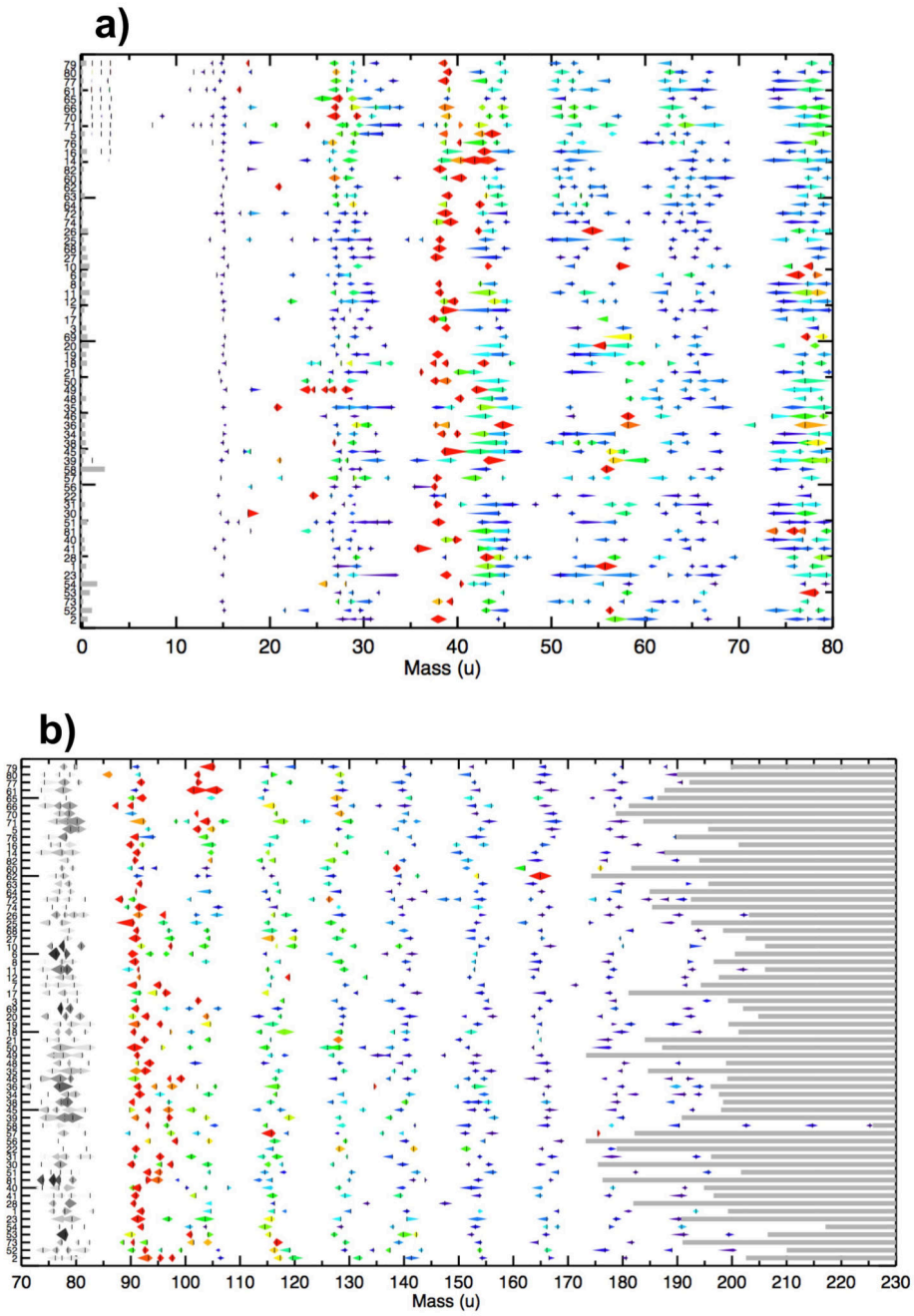

Extended Data Figure 1. semi-quantitative display of CDA HMOC spectra

All identified organic mass lines of individual HMOC spectra. Distribution of resolved mass lines and “flank peaks” of 64 HMOC spectra with the most distinct HMOC (Methods 1d). 19 further spectra with a high level of interference with water cluster ions or low signal to noise ratio are not included here (see ED Tab. 1). All peaks depicted here are also part of the statistics shown in Figure 1 of the main paper. The spectrum number “#” (as defined in ED Table 1) is indicated to the left as an identifier of the event. The extent and the relative

normalized amplitude of each spectral feature are indicated. The amplitude is given by the extension in the y-direction and the color code (red being the highest and blue the lowest amplitude). The largest horizontal diameter of the symbol marks the peak maximum. In the lower panel the amplitudes between of 70u to 85u are grey indicating that they are not to scale with the symbols shown at higher masses (they would be much larger, see Fig. 1b for comparison).

Spectra are sorted by their impact speed estimated from the orbital elements of the impinging grain, with the highest speed on top (≈ 15 km/s) and the lowest on the bottom (≈ 5 km/s). Since the exact orbital elements are unknown, each impact speed has substantial intrinsic uncertainties given in ED Tab. 1. The 12 spectra for which a minimum impact speed could be derived from the presence of hydrogen mass lines (ED Tab. 1, Methods 1d) are placed on top. The highest mass where the CDA TOF-spectrum recording ends varies between 174 u and 226 u (Methods 1a) and is indicated by the grey horizontal bars. As a consequence the frequency of the HMOC peaks around mass 178u and 191u is reduced in Figure 1b because not all individual spectra cover this mass range. The absolute masses in each individual spectrum have an intrinsic uncertainty of ±1u at 80, and ±2 u at 180 u due to the limited calibration accuracy of CDA in this high-mass regime. The mass intervals between peaks, however, are accurate to the integer level.

Europe PMC Funders Author Manuscripts

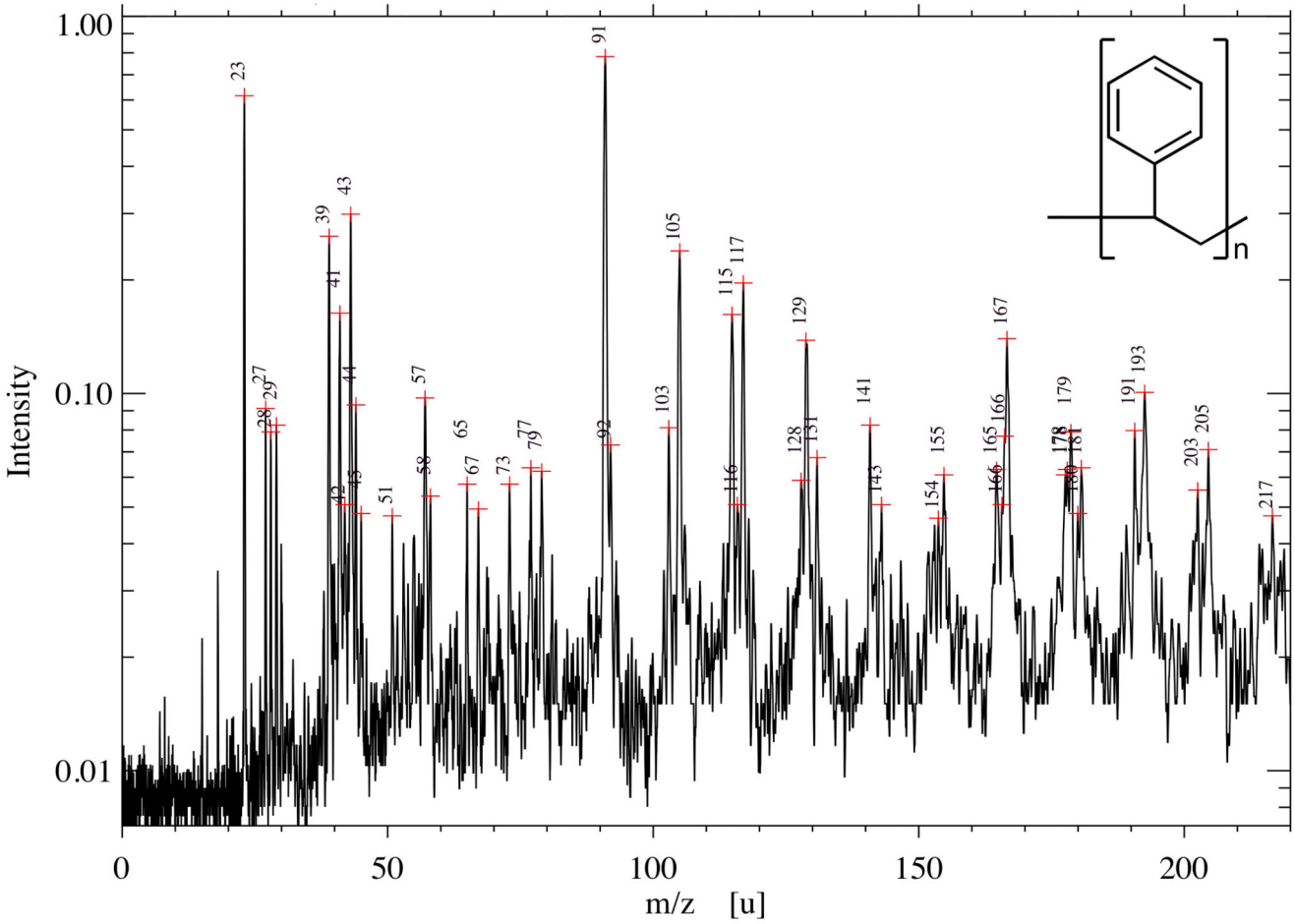

Extended Data Fig. 2. Impact ionization laboratory spectrum of a polystyrene (PS) bead
(modified from Fig. 5 in Srama et al., (2009)[19])

The impact ionization TOF mass spectrum of a PS particle with a radius of ≈ 1μm was recorded at the Heidelberg dust accelerator facility[36] with an impact speed of 5.2 km/s. Above 100 u and below 70 u the spectrum shows cationic fragments in good agreement with CDA HMOC spectra and the characteristic spacing of 12.5 u. The inset shows the molecular structure of the polymer. See main text and Methods 2 for further discussion.

Europe PMC Funders Author Manuscripts

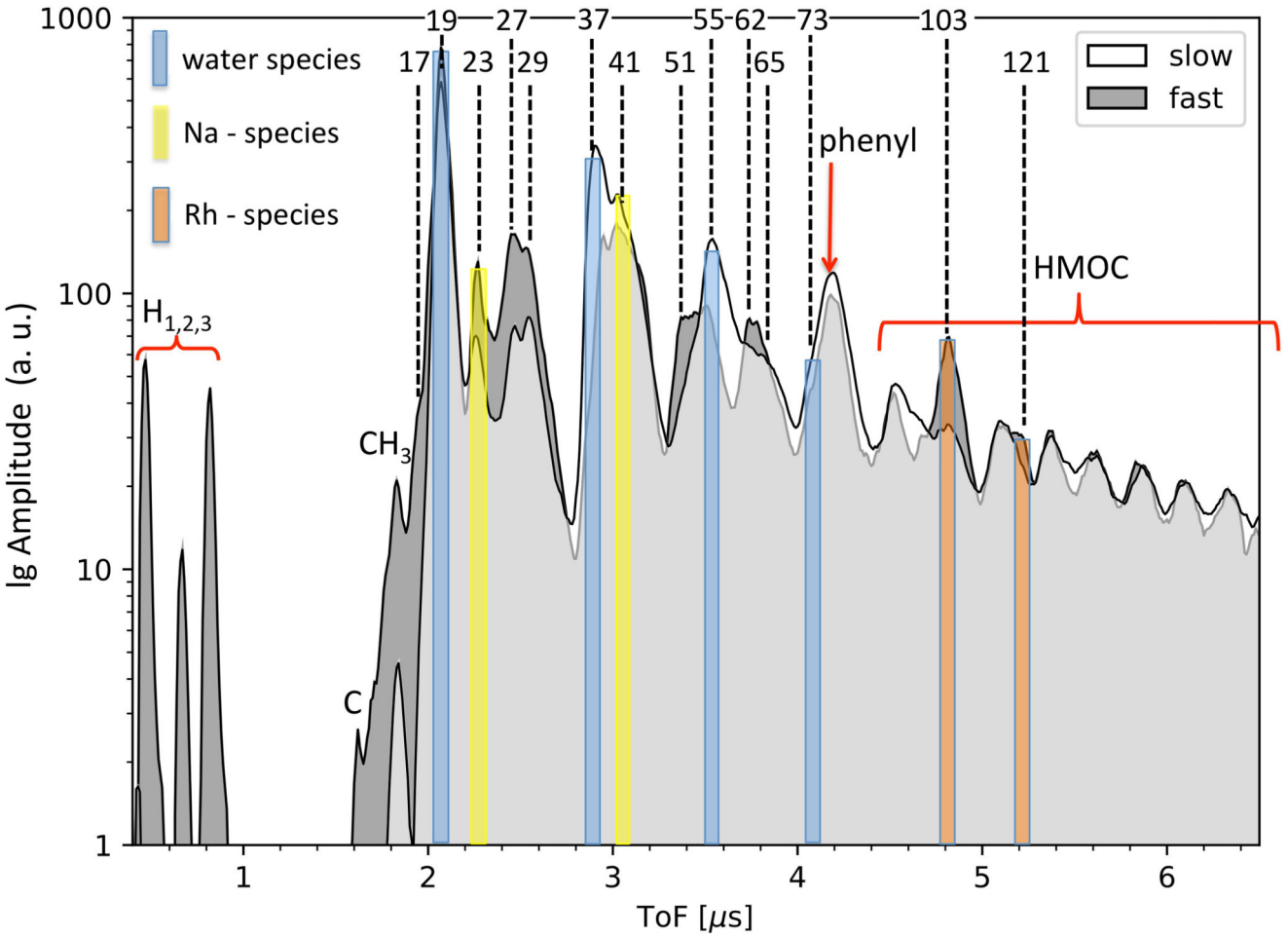

Extended Data Figure 3. Comparison of CDA HMOC spectra from 'fast' and 'slow' impacts

White and grey spectra represent the average of all spectra from impacts below and above ≈ 10 km/s, respectively (Methods 1d). All signatures with possible major contributions from inorganic species are color-shaded as in Fig. 1. All signatures not marked are exclusively or at least to a greater part due to organic cations.

The abundance and position of HMOC species is relatively independent of the impact speed of the ice grain (see also ED Fig. 1). In contrast, fast impacts induce stronger organic fragmentation signatures at masses below 70u and HMOC form more distinct, evenly spaced groups, which is characteristic of impact induced dissociation processes. In turn, slow impacts show more abundant intact benzene-like cations. There seems to be a tendency of some organic cations to carry less H-atoms at fast impacts (27 u, 51 u, 62 u) indicative of 'softer' ionization from the slower impact. In 'fast' spectra interference with water cluster ions is less frequent compared to lower speeds. In contrast to 'fast' spectra fragmentation below CH_3^+ (15u) is usually not observed in "slow" spectra. Spectra from slow impacts are prone to abundant water clustering, creating mass lines of the form $H^+(H_20)n$, n = 1 – 4 at 19 u, 37 u, 55 u, and 73 u (blue). In 'fast' spectra clustering is limited and only the mass lines at 19u and 37u are generally present; occasionally formation of smaller water ions OH^+ (17 u) and H_2O^+ (18 u) is observed. Similarly Rh^+(103 u) forms from excavation of the

impact target only at fast impacts and interferes with HMOC species there. To a lesser extent this is also true for the rhodium-water cluster $Rh^+(H_2O)$ at 121 u. See individual CDA spectra (ED Fig. 4) for comparison.

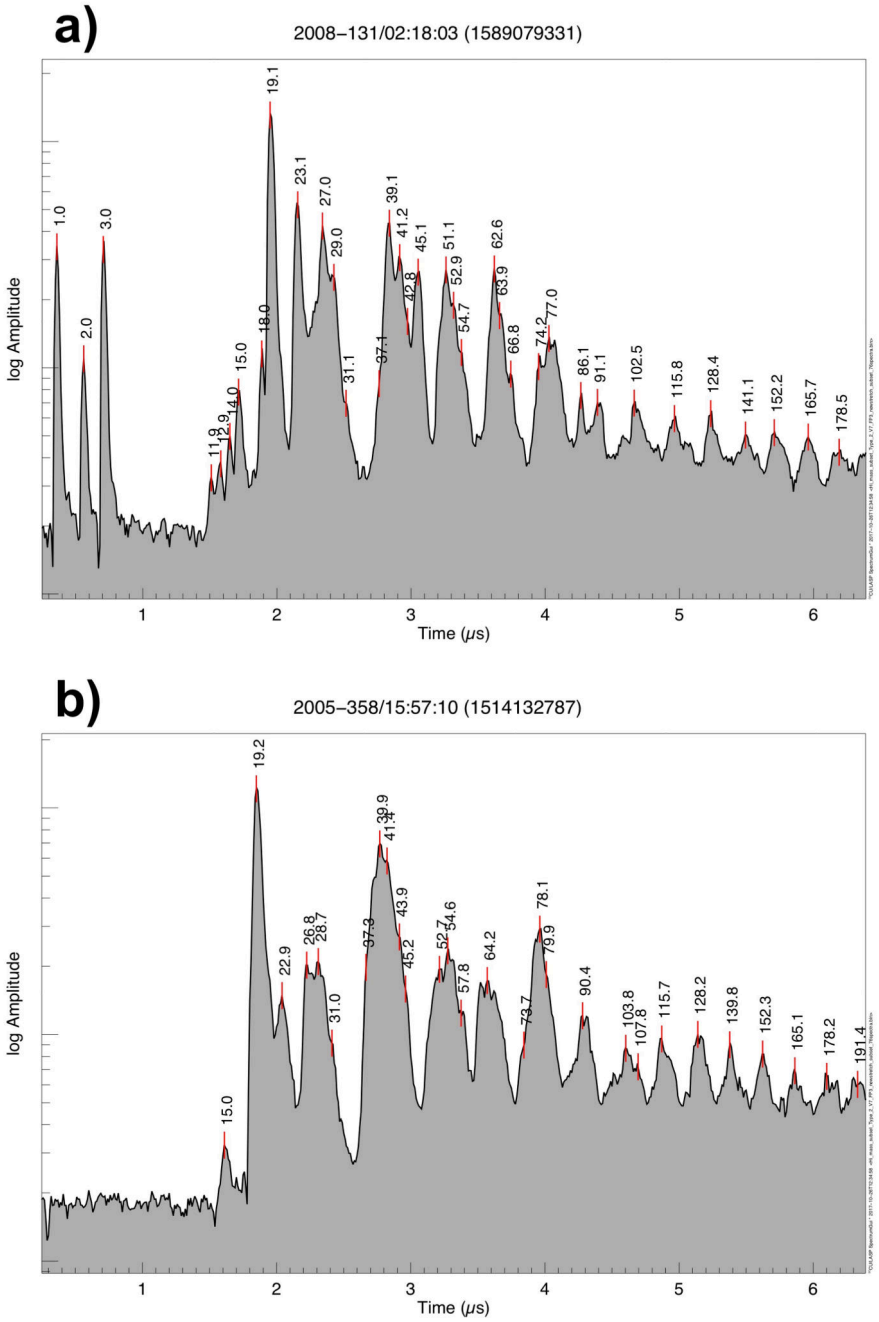

Extended Data Figure 4. CDA example spectra from individual HMOC-type ice grains

In these individual spectra the peak definition is naturally higher than in co-added spectra shown in Fig. 1 and ED Fig. 3 and therefore some of the spectral features collected in Fig. 1b become more apparent.

Europe PMC Funders Author Manuscripts

a) HMOC spectrum from one of the fastest recorded impacts (12 – 18 km/s. The appearances of hydrogen cations (H^+, H_2^+, H_3^+) at 1 u, 2 u, and 3 u as well as the disintegration of the CH_3^+ ion into CH_2^+, CH^+, and C^+ (12 – 15 u) and the formation of H_2O^+ (18 u) are witnesses of the high-speed impact. The abundance of unsaturated small cations below 70 u, probably fragments from aromatic structures, is increased compared to slower spectra. The frequently occurring mass line at 45u (Fig. 1b and ED Fig. 1) is quite noticeable. It cannot originate from pure hydrocarbons and requires heteroatoms, likely oxygen in this case. While a 45 u feature is quite common in our HMOC data set, the peak at 86 u is only apparent in this spectrum.

b) HMOC spectrum from a grain detected at intermediate speed (5 – 8 km/s). High mass fragments and benzene species are abundant whereas further fragmentation of the benzene ring into C_5 and C_4 species is less apparent compared to high velocity impacts (upper panel). Note, that organic cations with 2, 3, 4, and 5 C-atoms show the tendency to carry more H atoms compared with the high-speed impact indicative of ‘softer’ ionization from the slower impact. Organic fragmentation below CH_3^+ is usually not observed in this speed regime.

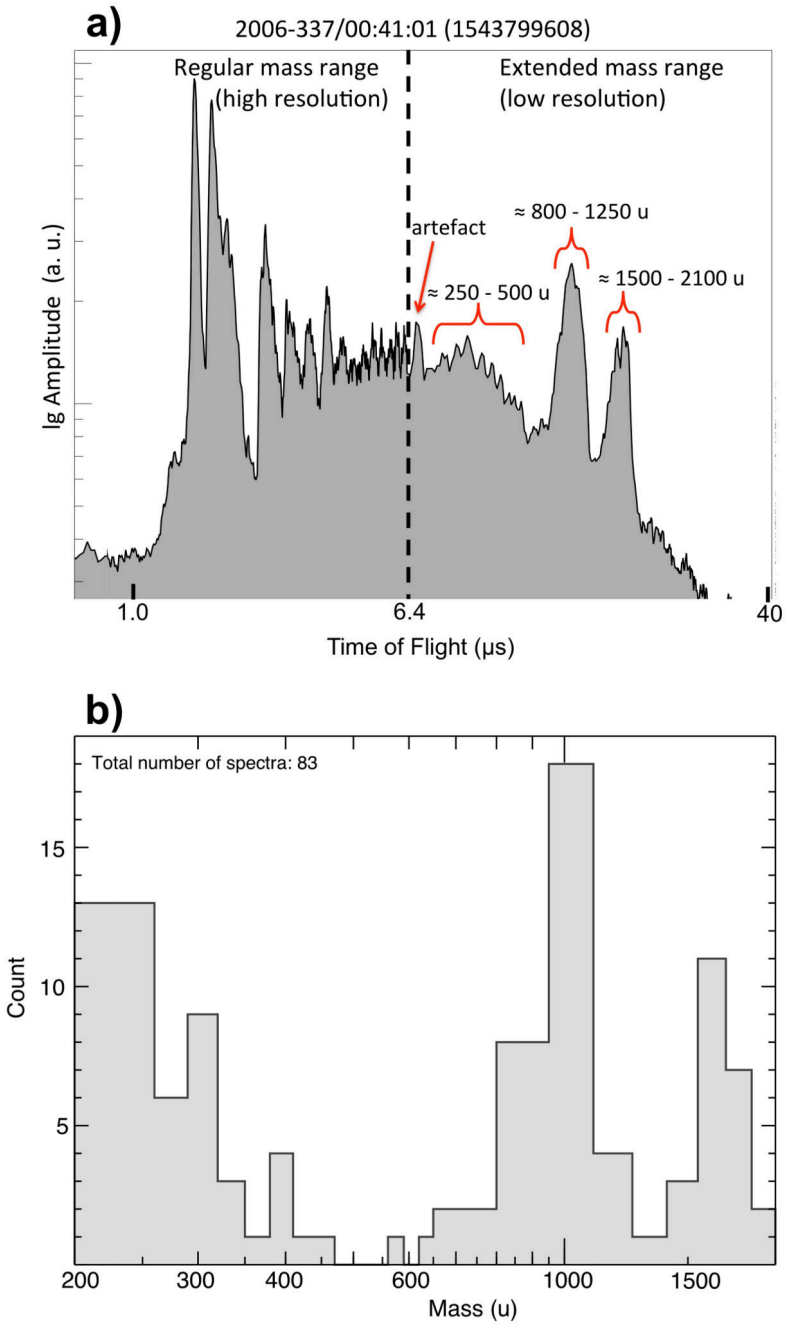

Extended Data Figure 5. HMOC example CDA mass spectrum with extended mass range and statistics of all features in the extended mass range

a) Ice grain spectrum showing the individual HMOC event with the strongest extended mass range signal of the data set. The dashed line at 6.4 µs divides the spectrum into the high-resolution part (10ns sampling) and the low-resolution part (100 ns sampling) (Methods 1a). There are several relatively narrow peaks between 250 u and 500 u and two much more extended features peaking at about 1000 u and 1800 u. In this case the cations in excess of 200 u are more than twice as abundant (defined by the area under the curve) as the ones below 200 u. Note the logarithmic x-axis is in this case. These features are usually less

frequent and less pronounced than in the extreme case shown in here. The extended spectrum frequently shows an instrument-artefact-peak at 6.8 μs not considered for our analysis.

b) Histogram showing the frequency of occurrences of features in the extended mass range. The definition and thus significance of peaks in the extended spectrum is generally lower than in the nominal spectrum. In particular, features above 500 u are sometimes ambiguous and their interpretation should be taken with great caution. However, the statistics shows three preferred mass regions: from 200 – 500 u with decreasing frequency, around 1000 u, and around 1700 u. Even if no significant peaks are present, the cation signal in HMOC spectra is generally in excess of the noise level when the low-resolution recording starts and typically only decays to noise level at around 500u or later.

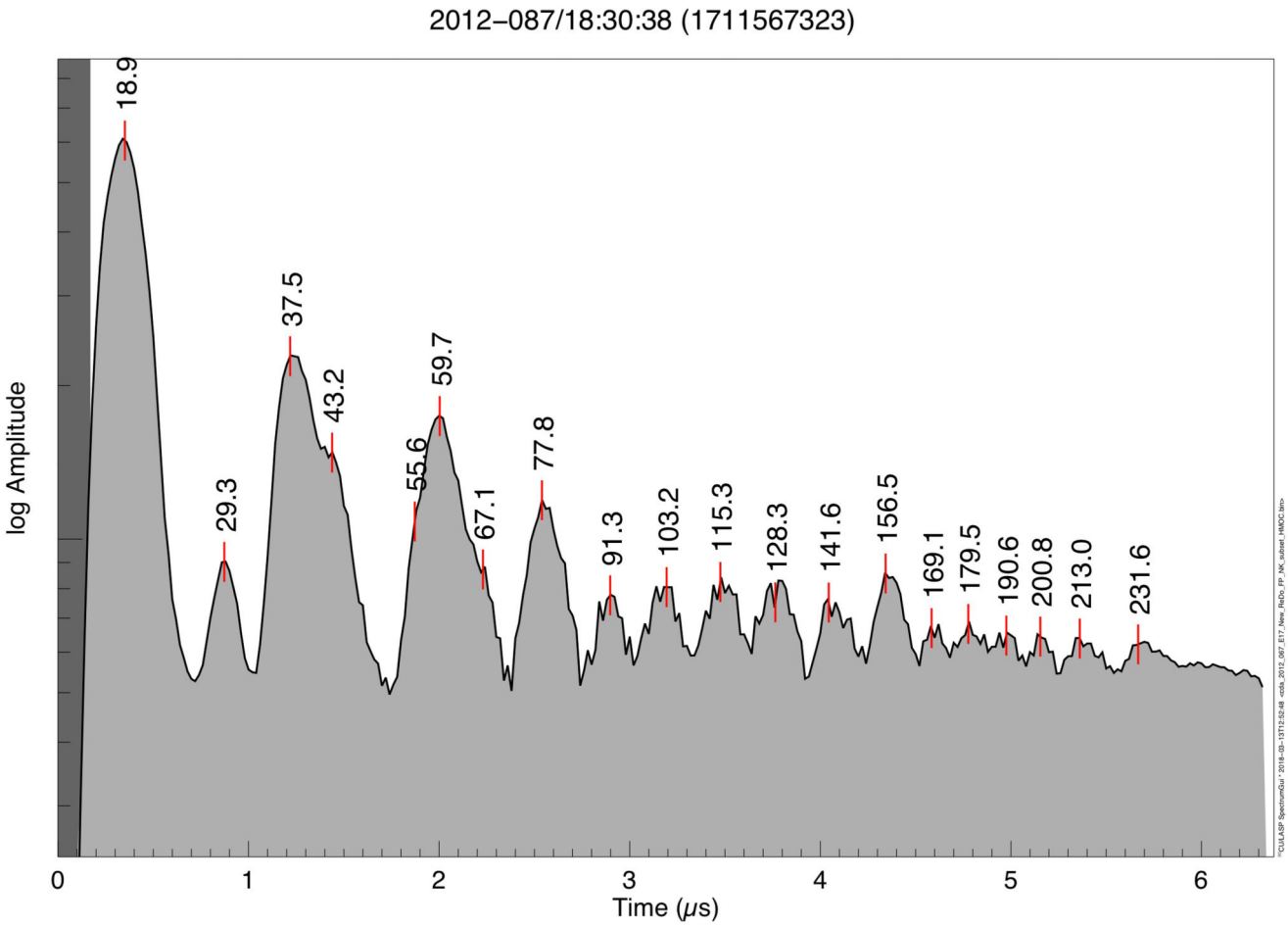

Extended Data Fig. 6. CDA HMOC spectrum recorded in Enceladean plume

During Cassini's E17 south polar Enceladus flyby at 75km altitude, where CDA recorded about 40 plume spectra with its full mass range, one spectrum was of the HMOC type. This is in agreement with a proportion of this particle type of a few percent in the plume and in the E ring close to Enceladus (Methods 1c). The impact speed was 8.6 km/s and the particle was about 2 μm in radius. In order to operate the CDA in the dense dust environment of the

plume the instrument settings had to be modified in a way that it compromised the spectrum quality (lower sensitivity and lower mass resolution, see ED Fig.4 for comparison). The spectrum is baseline corrected.

During the only occasion where CDA recorded a large number of spectra with high cadence directly in the plume during Cassini's E5 flyby, the spectral range was truncated below about 100 u to allow for a higher data rate. This unfortunately did not allow the identification of the defining HMOC signatures.

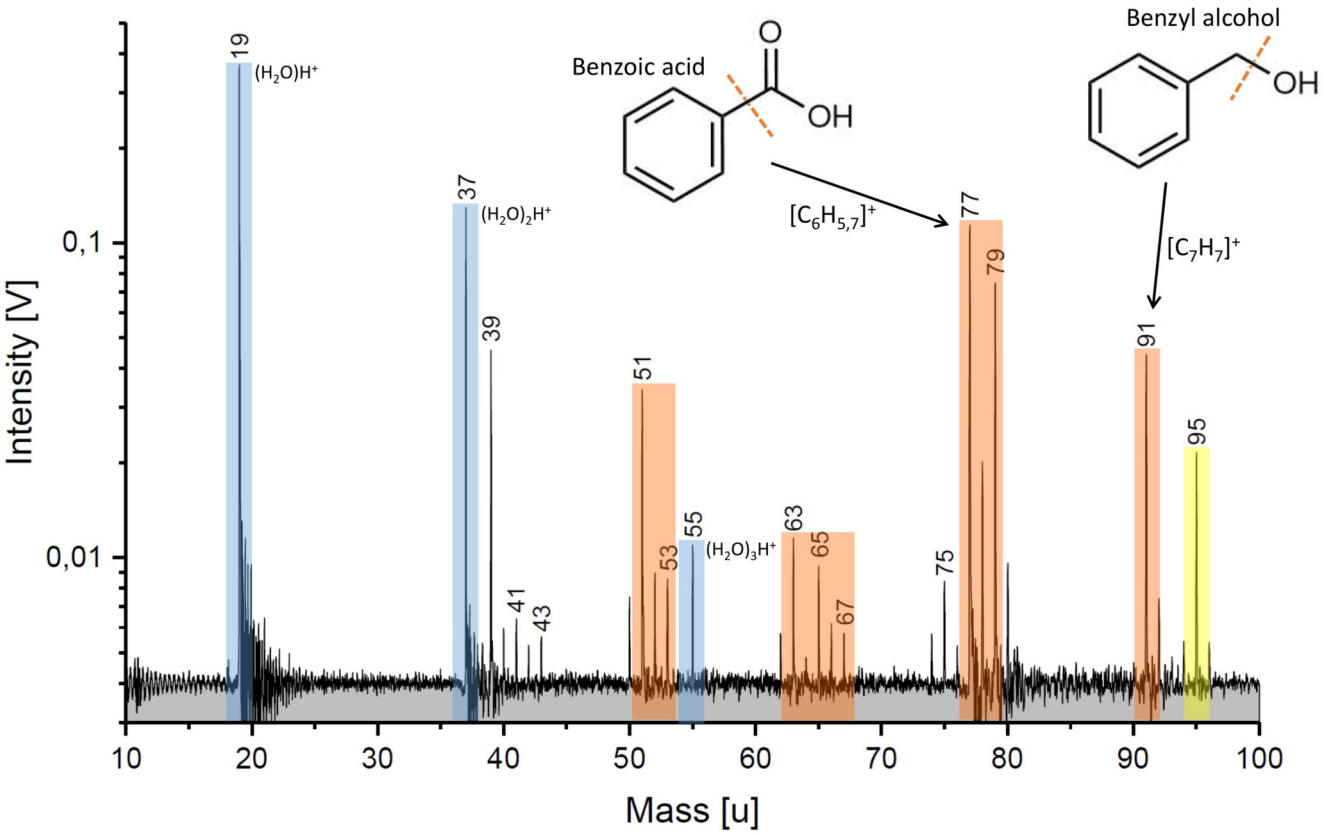

Extended Data Figure 7. Laser ionization mass spectrum of benzoic acid and benzyl alcohol dissolved in water.

Analog TOF mass spectrum recorded with the liquid micro beam ionization setup (Methods 8 and ED Fig. 9) to simulate the formation of tropylium and benzene cations and their fragmentation ions at impact speeds in the order of 10 km/s [78]. Concentration of bezoic acid and benzyl alcohol are 3 g/l and 0.2 g/l, respectively. Water ions are marked in blue, aromatic ions and ions from aromatic fragmentation are marked orange, mixed organic / water species are yellow.

In order to yield both, benzene cations (77 u – 79 u) and tropylium ions (91 u), two different aromatic structures are required (Figure 2). Whereas the predominant aromatic fragments of benzoic acid are at 77 u and 79 u, benzyl alcohol almost exclusively forms tropylium ions at 91 u. The peak at 95 u is a water cluster of the phenyl cation, which is much more pronounced than in HMOC spectra. Whereas the strong phenyl-water cluster signature here illustrates the intimate mixing of organics with water, the much lower 95u signature in

Europe PMC Funders Author Manuscripts

HMOC spectra argues for less efficient mixing of organics with water there, probably due to a core shell/structure that physically separates organics from ice in the grain.

Cations from the fragmented ring can be seen at 39 u, 51 - 53 u and 63 – 65 u and agree with the CDA observations (Figure 1b). In contrast to the CDA spectra, however, saturated C_3 fragments (41 u – 43 u) are depleted and C_2 (27 – 29 u) and C_1 (15 u) fragment cations are entirely absent, confirming the presence of an abundance of aliphatic cations in HMOC grains.

The ratios of benzene and tropylium ions on one hand and the water ions on the other hand match the HMOC spectra quite well. The total concentration of organic species used here (≈ 0.32 % by weight) can be used to estimate a lower limit for the concentration of organics in CDA HMOC grains for two reasons. First, in the analog experiment we selected substances that most efficiently yield the desired aromatic species, and other less efficient precursors would yield even lower signals at 77 u and 91 u. Second, to account for both the low and high mass fragments between 100 u and 2000 u, which are absent in the lab spectrum, additional organic substances and/or larger molecules, would be needed to further increase the organic concentration. Therefore, the concentration in Enceladean HMOC ice grains in many cases can be estimated to be near or even above the percent level.

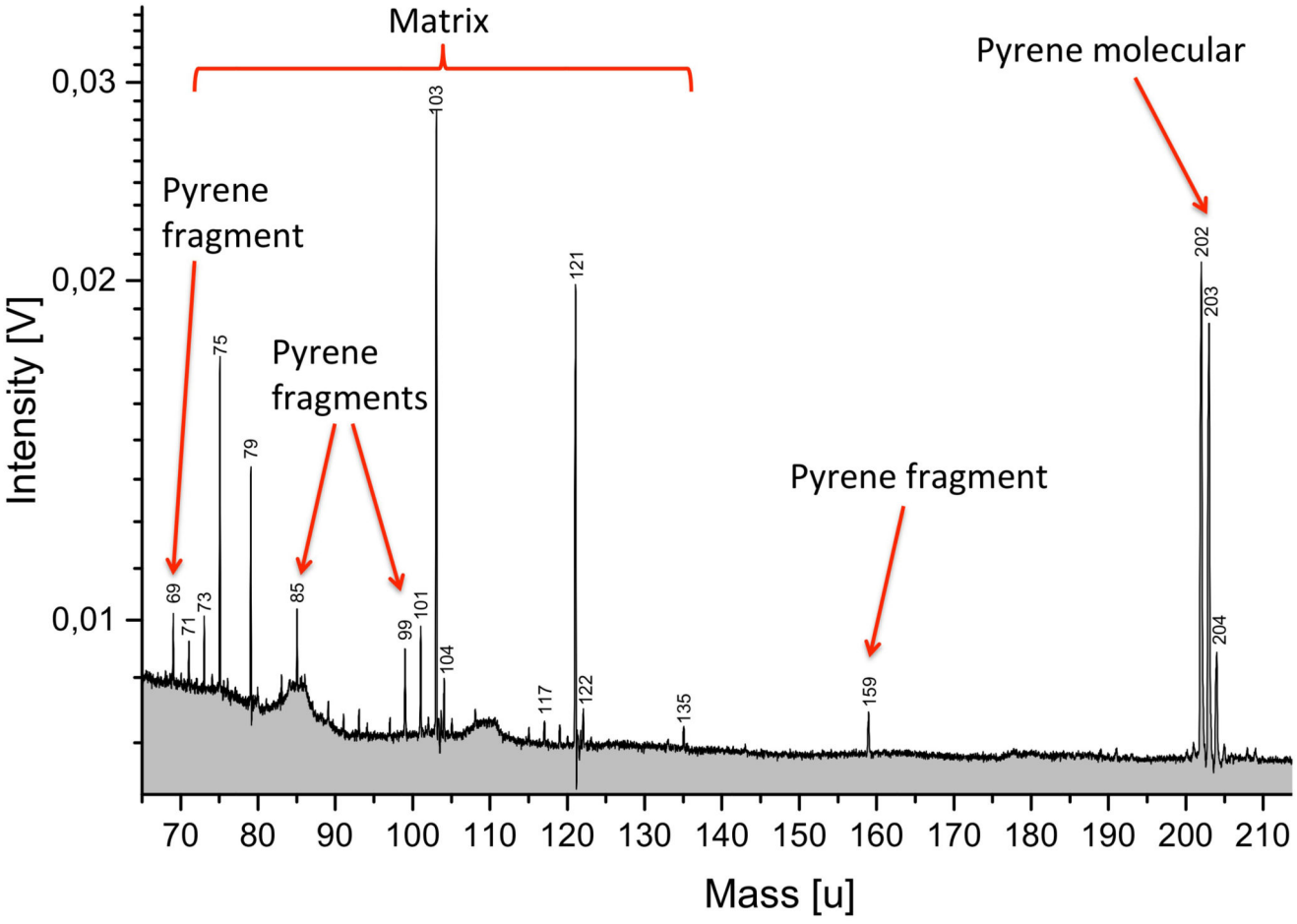

Extended Data Figure 8. Laser ionization analogue spectrum of pyrene in water/acetic acid

Cationic TOF mass spectrum recorded with the liquid microbeam ionization setup (Methods 8, ED Fig. 9) containing 0.1 % pyrene dissolved in a mixture of water and acetic acid. The laser pulse simulates an ice grain impact with a speed of about 10 km/s [78]. All features marked as “pyrene fragment” do not appear up in the blank experiment with just the solvent mixture and are either direct pyrene fragments or cations formed from pyren fragments clustering with the solvent (e.g. at 159 u).

The molecular mass lines of pyrene are about 10 times more abundant than any fragments, indicating the stability of the PAH molecule. An isolated benzene ring fragment (77 u or 91 u) as in CDA HMOC spectra does not form.

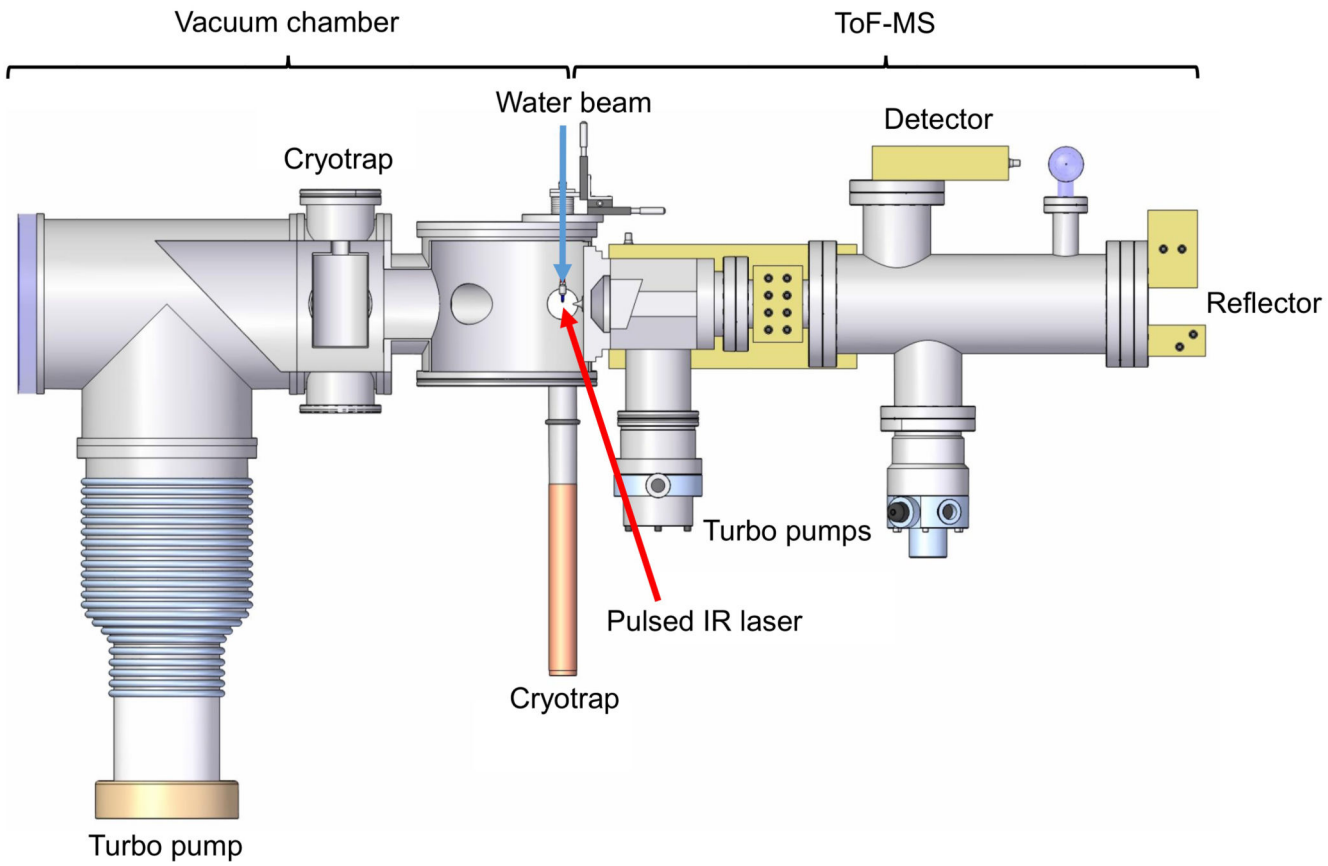

Extended Data Figure 9. Laboratory setup to simulate ice grain impacts onto spaceborne impact ionization detectors.

See Methods 8 for a detailed description.

Europe PMC Funders Author Manuscripts

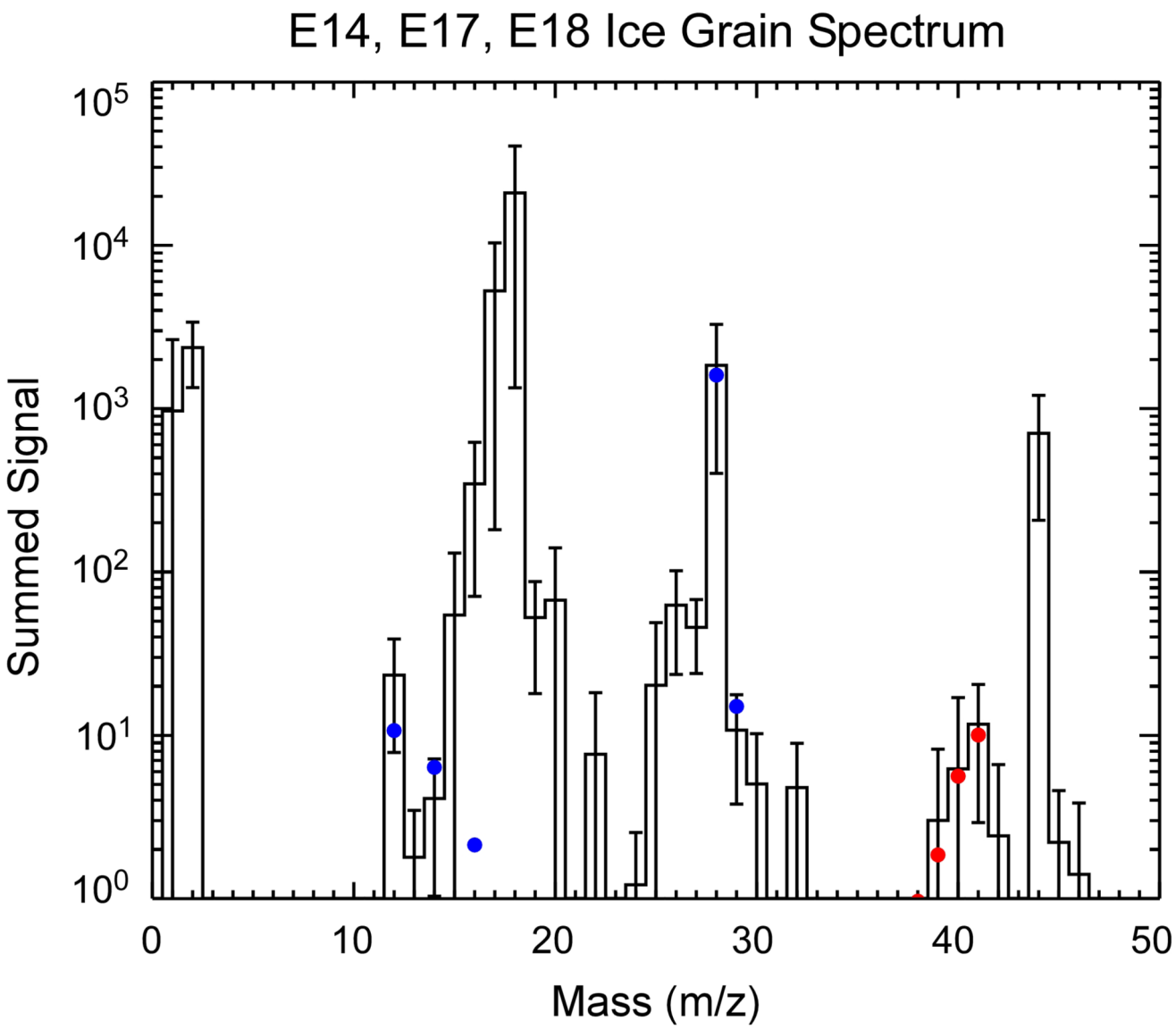

Extended Data Figure 10. Co-added INMS ice grain spike spectrum from three plume encounters

See Methods 3b for details on how the spectrum was composed and details of its analysis. Error bars are derived from the dispersion of the count rate from the three encounters. The spectrum suggests the presence of CO fragments (blue circles) as an oxygen bearing species: N_2 has very low abundance and contributes <~10% of the 28u signal. CO_2 and C_2H_4 collectively contribute <~10% of the 28u signal. CO (blue circles) is required to fit the rest of the 28u signal and matches its other dissociative peaks well. The spectrum also indicates the presence of nitrogen-bearing species: the ‘stairstep' pattern around 41u matches best to the C_2H_3N spectrum (red circles). The error bars are one standard deviation, calculated from the three separate measurements of the individual encounters.

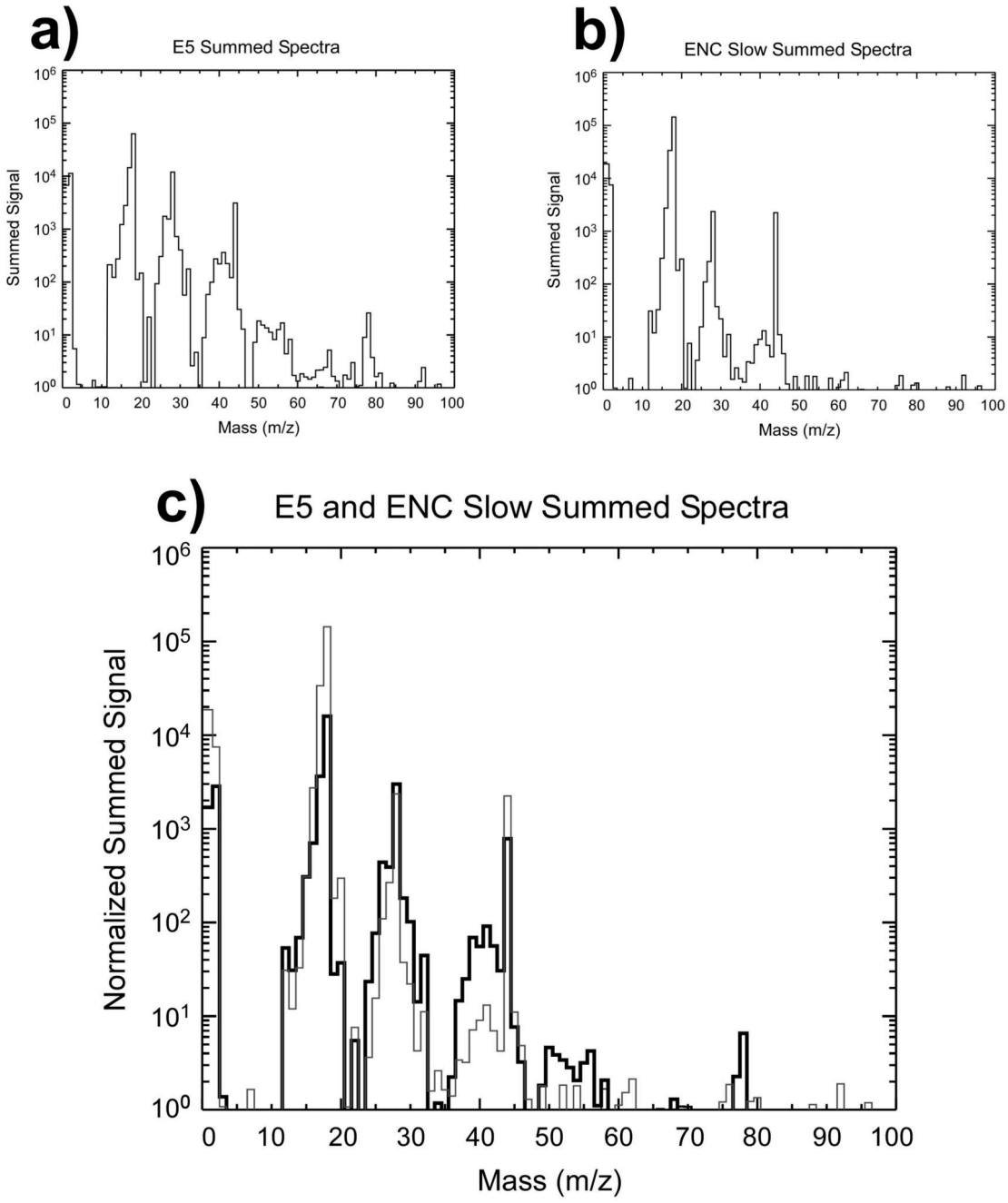

Extended Data Figure 11. INMS Spectra used to produce the differenced spectrum in Fig. 3

The individual spectra for fast (E5) (a) and slow flybys (b) are shown in the upper panel. Below both spectra have been overplotted (c) with E5 (black) normalized so that it matches the 15u signal of the "slow" spectrum (grey). The residual (difference) between the two spectra is plotted in Fig. 3.

Europe PMC Funders Author Manuscripts

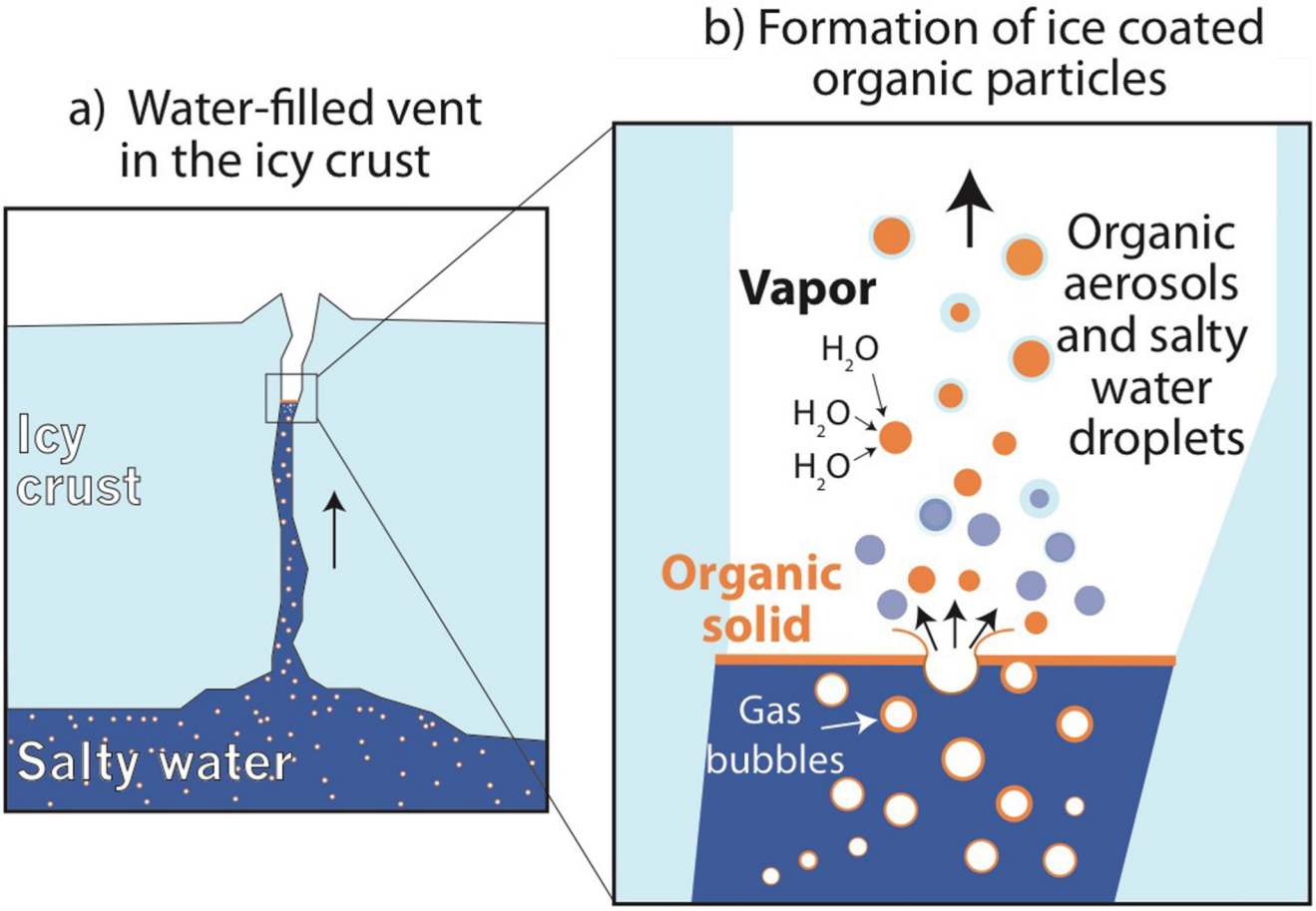

Extended Data Figure 12. Schematic on the formation of organic condensation cores from an refractory organic film

Ascending gas bubbles in the ocean efficiently transport organic material[30] into water filled cracks in the south polar ice crust (a). Organics ultimately concentrate in a thin organic layer (orange) on top of the water table located inside the icy vents. When gas bubbles burst, they form aerosols made of insoluble organic material that later serve as efficient condensation cores for an icy crust from water vapor thereby forming HMOC-type particles (b). In parallel, larger, pure salt-water droplets form (blue), which freeze and are later detected by CDA as salt-rich Type 3 ice particles in the plume[8,9].

Europe PMC Funders Author Manuscripts

Extended Data Table 1
83 CDA mass spectra identified as of HMOC type.

Columns of the table are, number (in order of detection), Coordinated Universal Time (UTC), Spacecraft clock, amplitude of CDA ion grid charge (QI channel) (C), spacecraft distance to Saturn's rotation axis (in Saturn radii, R_S = 60,268 km), spacecraft distance to the ring plane (R_S), grain impact speeds (in km/s, 3 columns), and corresponding radii estimates (in μm, 3 columns). For the grain impact speeds, V_{imp} is derived assuming grains are in circular Keplerian orbits. $V_{-\sigma}$ and $V_{+\sigma}$ are the ±1σ of the grain impact speed distributions derived using the numerical E ring dynamics mode[74]. The grain radii shown in the last three columns are calculated based on V_{imp}, $V_{-\sigma}$, and $V_{+\sigma}$ using equation 3.37 in Srama (2009)[79].

The events where the UTC is shown in bold face are the 64 spectra selected as high quality (Methods 1d). The speeds marked with an asterisk are the spectra where one or more hydrogen cations (H^+, H_2^+, H_3^+) are present, which is used as an independent criterion for impact speeds larger than 10 km/s (Methods 1d).

#	UTC	SCLK	QI (C)	R (R_s)	Z (R_s)	V_{imp}	$V_{-\sigma}$	$V_{+\sigma}$	Radius (μm)		
1	**2004-302/21:31:38**	1477691821	1.34E-14	8.6	-0.22	6.4	4.7	8.0	0.8	0.3	2
2	**2005-068/12:11:47**	1489063103	4.04E-14	3.53	0.01	5.0	3.7	6.3	1.2	0.5	3.2
3	**2005-068/19:12:50**	1489088367	2.30E-14	6.24	0.02	8.4	6.2	10.6	0.6	0.2	1.5
4	2005-068/19:57:18	1489091035	5.29E-14	6.61	0.02	8.4	6.2	10.6	0.7	0.3	1.7
5	**2005-177/09:15:19**	1498470176	1.02E-13	5.68	-1.44	8.6*	6.4	10.9	0.7	0.3	1.9
6	**2005-177/09:16:46**	1498470263	4.43E-14	5.67	-1.44	8.6	6.4	10.9	0.6	0.3	1.6
7	**2005-177/10:14:42**	1498473739	1.68E-13	5.21	-1.13	8.7	6.4	11.0	0.7	0.3	2
8	**2005-177/10:15:39**	1498473796	2.55E-14	5.2	-1.13	8.7	6.4	11.0	0.6	0.2	1.5
9	2005-177/10:19:23	1498474020	1.32E-14	5.18	-1.11	8.7	6.4	11.0	0.5	0.2	1.4
10	**2005-177/10:23:56**	1498474293	1.62E-14	5.14	-1.08	8.7	6.4	11.0	0.5	0.2	1.4
11	**2005-177/11:24:38**	1498477935	2.12E-14	4.69	-0.74	8.6	6.4	10.9	0.6	0.2	1.5
12	**2005-177/11:36:22**	1498478639	2.88E-14	4.61	-0.67	8.6	6.4	10.9	0.6	0.2	1.5
13	2005-177/11:46:21	1498479238	1.40E-14	4.54	-0.62	8.6	6.4	10.9	0.5	0.2	1.4
14	**2005-177/12:00:40**	1498480097	5.02E-14	4.45	-0.53	8.6*	6.3	10.8	0.6	0.3	1.7
15	2005-177/12:22:55	1498481432	5.43E-14	4.3	-0.4	8.5*	6.3	10.7	0.6	0.3	1.7
16	**2005-177/12:24:48**	1498481545	2.54E-14	4.29	-0.39	8.5*	6.3	10.7	0.6	0.2	1.5
17	**2005-177/12:31:51**	1498481968	3.26E-14	4.25	-0.35	8.5	6.3	10.7	0.6	0.3	1.6
18	**2005-177/12:48:40**	1498482977	1.10E-14	4.15	-0.25	8.4	6.2	10.6	0.5	0.2	1.4
19	**2005-177/12:49:08**	1498483005	4.12E-14	4.15	-0.24	8.4	6.2	10.6	0.6	0.3	1.7
20	**2005-177/12:50:33**	1498483090	1.82E-14	4.14	-0.24	8.4	6.2	10.6	0.6	0.2	1.5
21	**2005-177/12:56:32**	1498483449	5.27E-14	4.11	-0.2	8.3	6.2	10.5	0.7	0.3	1.8
22	**2005-177/15:48:06**	1498493743	2.20E-14	3.61	0.81	6.9	5.1	8.7	0.7	0.3	1.9
23	**2005-177/16:47:37**	1498497314	3.55E-13	3.69	1.11	6.6	4.9	8.3	1.2	0.5	3.1
24	2005-267/03:21:33	1506224999	3.40E-14	5.24	0.01	9.1	6.8	11.5	0.6	0.2	1.5

Europe PMC Funders Author Manuscripts

#	UTC	SCLK	QI (C)	R (R_S)	Z (R_S)	V_{imp}	$V_{-\sigma}$	$V_{+\sigma}$	Radius (μm)		
25	**2005-267/03:22:22**	1506225048	9.24E-14	5.25	0.01	9.2	6.8	11.5	0.6	0.3	1.7
26	**2005-267/03:35:30**	1506225836	2.75E-14	5.37	0.01	9.2	6.8	11.6	0.5	0.2	1.4
27	**2005-267/07:34:31**	1506240177	2.94E-14	7.52	0	8.8	6.5	11.2	0.6	0.2	1.5
28	**2005-303/04:28:34**	1509339440	3.74E-14	5.76	0.04	6.4	4.8	8.1	0.9	0.4	2.3
29	2005-303/04:43:14	1509340320	1.75E-14	5.85	0.04	6.5	4.8	8.2	0.8	0.3	2
30	**2005-303/04:48:04**	1509340610	4.42E-14	5.88	0.04	6.6	4.8	8.3	0.9	0.4	2.3
31	**2005-303/05:03:27**	1509341533	4.64E-14	5.98	0.04	6.6	4.9	8.4	0.9	0.4	2.3
32	2005-303/05:43:23	1509343929	4.32E-14	6.24	0.04	6.8	5.0	8.6	0.8	0.3	2.2
33	2005-303/05:53:09	1509344515	5.82E-13	6.3	0.04	6.8	5.1	8.6	1.2	0.5	3.2
34	**2005-303/05:59:07**	1509344873	7.83E-14	6.34	0.04	6.9	5.1	8.7	0.9	0.4	2.4
35	**2005-303/06:36:17**	1509347103	3.31E-13	6.59	0.04	7.0	5.2	8.8	1.1	0.4	2.9
36	**2005-303/06:41:04**	1509347390	8.31E-14	6.62	0.04	7.0	5.2	8.8	0.9	0.4	2.3
37	2005-330/22:05:55	1511735696	2.39E-14	8.97	-0.06	7.3	5.4	9.2	0.7	0.3	1.8
38	**2005-358/14:37:41**	1514128018	6.68E-14	6.2	-0.03	6.8	5.0	8.6	0.9	0.4	2.3
39	**2005-358/14:49:12**	1514128709	4.32E-13	6.13	-0.03	6.8	5.0	8.5	1.2	0.5	3.1
40	**2005-358/15:57:10**	1514132787	2.07E-14	5.71	-0.02	6.4	4.7	8.1	0.8	0.3	2.1
41	**2005-358/15:57:39**	1514132816	4.30E-14	5.7	-0.02	6.4	4.7	8.1	0.9	0.4	2.4
42	2005-358/16:09:40	1514133537	7.77E-15	5.63	-0.02	6.3	4.7	8.0	0.7	0.3	1.8
43	2005-359/03:01:39	1514172656	6.11E-13	5.78	0.04	6.5	4.8	8.2	1.3	0.5	3.5
44	2005-359/04:06:40	1514176557	2.87E-14	6.19	0.04	6.8	5.0	8.6	0.8	0.3	2.1
45	**2005-359/04:06:52**	1514176569	9.60E-14	6.19	0.04	6.8	5.0	8.6	0.9	0.4	2.5
46	**2005-359/05:10:40**	1514180397	5.38E-14	6.62	0.04	7.0	5.2	8.8	0.8	0.3	2.2
47	2005-359/05:20:58	1514181015	4.33E-14	6.69	0.05	7.0	5.2	8.9	0.8	0.3	2.1
48	**2005-359/06:01:55**	1514183472	2.19E-14	6.98	0.05	7.1	5.3	9.0	0.7	0.3	1.9
49	**2005-359/06:26:12**	1514184929	7.14E-14	7.15	0.05	7.2	5.3	9.0	0.8	0.3	2.2
50	**2005-359/06:32:15**	1514185292	1.35E-13	7.19	0.05	7.2	5.3	9.0	0.9	0.4	2.4
51	**2006-016/08:08:18**	1516091868	5.75E-14	12.91	-0.08	6.5	4.8	8.2	0.9	0.4	2.4
52	**2006-056/05:15:38**	1519537530	1.26E-14	6.46	-0.03	5.4	4.0	6.8	0.9	0.4	2.4
53	**2006-056/17:46:16**	1519582569	1.65E-14	6.82	0.04	5.7	4.2	7.2	0.9	0.4	2.3
54	**2006-056/18:48:22**	1519586295	9.86E-15	7.15	0.04	6.0	4.4	7.5	0.8	0.3	2
55	2006-056/22:14:58	1519598691	1.32E-14	8.4	0.05	6.5	4.8	8.1	0.7	0.3	1.9
56	**2006-057/02:02:07**	1519612320	6.24E-14	9.88	0.07	6.6	4.9	8.4	0.9	0.4	2.4
57	**2006-057/02:05:38**	1519612531	3.55E-14	9.9	0.07	6.6	4.9	8.4	0.8	0.3	2.2
58	**2006-080/15:29:58**	1521648004	1.64E-14	11.6	0.08	6.7	4.9	8.4	0.7	0.3	1.9
59	2006-080/19:20:46	1521661852	1.79E-14	13.1	0.09	6.5	4.8	8.2	0.8	0.3	2
60	**2006-337/00:41:01**	1543799608	8.17E-14	4.99	0.04	12.6	9.3	15.8	0.4	0.2	1.1
61	**2006-337/00:46:46**	1543799953	4.60E-13	5.01	0.11	12.5*	9.3	15.8	0.5	0.2	1.4
62	**2006-337/00:55:19**	1543800466	4.77E-14	5.04	0.21	1.7	1.3	2.1	0.4	0.2	1.1
63	**2006-337/00:59:05**	1543800692	1.55E-14	5.05	0.25	12.5	9.2	15.8	0.3	0.1	0.9

#	UTC	SCLK	QI (C)	R (R_S)	Z (R_S)	V_{imp}	$V_{-\sigma}$	$V_{+\sigma}$	Radius (μm)		
64	**2006-337/01:18:39**	1543801866	1.86E-14	5.13	0.48	12.4	9.2	15.6	0.4	0.1	0.9
65	**2006-337/01:26:38**	1543802345	3.85E-14	5.16	0.57	12.4*	9.1	15.6	0.4	0.2	1
66	**2006-337/04:59:37**	1543815124	1.57E-13	6.24	2.93	10.6*	7.8	13.3	0.6	0.2	1.5
67	2006-337/05:49:38	1543818125	1.75E-14	6.54	3.43	10.1	7.5	12.8	0.4	0.2	1.2
68	**2006-349/04:52:09**	1544851483	4.86E-14	7.89	-2.66	8.9	6.5	11.2	0.6	0.2	1.6
69	**2006-349/16:06:48**	1544891962	3.95E-14	10.08	2.6	8.3	6.1	10.5	0.6	0.3	1.7
70	**2007-130/19:21:23**	1557518117	8.31E-14	4.8	0.08	10.3*	7.6	13.0	0.5	0.2	1.5
71	**2007-130/19:32:19**	1557518773	5.98E-13	4.75	-0.02	10.3*	7.6	13.0	0.7	0.3	1.9
72	**2007-130/19:37:15**	1557519069	4.10E-14	4.73	-0.06	10.3	7.6	13.0	0.5	0.2	1.3
73	**2007-130/19:44:45**	1557519519	6.15E-14	4.7	-0.13	10.3	7.6	13.0	0.5	0.2	1.4
74	**2007-130/19:50:29**	1557519863	3.34E-14	4.68	-0.18	10.3	7.6	13.0	0.5	0.2	1.3
75	2007-130/19:51:50	1557519944	1.49E-13	4.67	-0.2	10.3	7.6	13.0	0.6	0.2	1.6
76	**2007-130/19:53:50**	1557520064	3.66E-14	4.66	-0.21	10.3*	7.6	12.9	0.5	0.2	1.3
77	**2008-130/23:08:03**	1589067930	1.16E-13	4.67	0.76	14.3*	10.6	18.0	0.4	0.2	1
78	2008-130/23:57:13	1589070880	2.02E-14	4.5	0.1	14.6*	10.8	18.5	0.3	0.1	0.8
79	**2008-131/00:20:35**	1589072282	4.29E-14	4.44	-0.21	14.7*	10.9	18.6	0.3	0.1	0.9
80	**2008-131/02:18:04**	1589079331	5.10E-14	4.3	-1.75	14.1*	10.4	17.8	0.3	0.1	0.9
81	**2008-131/03:00:00**	1589081847	8.66E-14	4.32	-2.26	13.5	10.0	17.0	0.4	0.2	1
82	**2008-131/03:16:31**	1589082838	1.34E-13	4.35	-2.46	13.2	9.8	16.7	0.4	0.2	1.1
83	2008-131/03:19:14	1589083001	6.43E-14	4.35	-2.49	13.2*	9.7	16.6	0.4	0.2	1

Acknowledgements

The research leading to these results received financial support from German Research Foundation DFG projects PO 1015/2-1, /3-1, /4-1 and ERC Consolidator Grant 724908 — Habitat-OASIS (F.P., N.K, L.N., F.K., R.R.), AB 63/9-1 (B.A., F.S.), the Klaus Tschira Stiftung (M.T., F.P.), NASA contract NAS703001TONMO71123, JPL subcontract 1405853 (J.H.W., C.R.G, B.M.), INMS science support grant NNX13AG63G (M.P.), NASA Habitable Worlds Program, JPL's RTD funding (M.S.G., B.L.H.).

References

1. Thomas PC, et al. Enceladus's measured physical libration requires a global subsurface ocean. Icarus. 2016; 264:37–47.
2. Iess L, et al. The Gravity Field and Interior Structure of Enceladus. Science. 2014; 344:78–80. [PubMed: 24700854]
3. Spencer JR, et al. Cassini Encounters Enceladus: Background and the Discovery of a South Polar Hot Spot. Science. 2006; 311:1401–1405. [PubMed: 16527965]
4. Spahn F, et al. Cassini dust measurements at Enceladus and implications for the origin of the E ring. Science. 2006; 311:1416–1418. [PubMed: 16527969]
5. Porco CC, et al. Cassini Observes the Active South Pole of Enceladus. Science. 2006; 311:1393–1401. [PubMed: 16527964]
6. Waite JH Jr, et al. Cassini ion and neutral mass spectrometer: Enceladus plume composition and structure. Science. 2006; 311:1419–1422. [PubMed: 16527970]
7. Hansen CJ, et al. Enceladus Water Vapor Plume. Science. 2006; 311:1422–1425. [PubMed: 16527971]

8. Postberg F, et al. Sodium salts in E-ring ice grains from an ocean below the surface of Enceladus. Nature. 2009; 459:1098–1101. [PubMed: 19553992]
9. Postberg F, Schmidt J, Hillier J, Kempf S, Srama R. A salt-water reservoir as the source of a compositionally stratified plume on Enceladus. Nature. 2011; 474:620–622. [PubMed: 21697830]
10. Hsu S, et al. Ongoing hydrothermal activities within Enceladus. Nature. 2015; 519:207–210. [PubMed: 25762281]
11. Sekine Y, et al. High-temperature water-rock interactions and hydrothermal environments in the chondrite-like core of Enceladus. Nat Commun. 2015; 6:8604. [PubMed: 26506464]
12. Waite JH Jr, et al. Cassini finds molecular hydrogen in the Enceladus plume: Evidence for hydrothermal processes. Science. 2017; 356:155–159. [PubMed: 28408597]
13. Choblet G, et al. Powering prolonged hydrothermal activity inside Enceladus. Nature Astronomy. 2017; 1:841–847.
14. Postberg F, et al. The E ring in the vicinity of Enceladus. II. Probing the moon's interior—the composition of E-ring particles. Icarus. 2008; 193:438–454.
15. Waite JH Jr, et al. Liquid water on Enceladus from observations of ammonia and 40Ar in the plume. Nature. 2009; 460:487–490.
16. Kempf S, Beckmann U, Schmidt J. How the Enceladus dust plume feeds Saturn's E ring. Icarus. 2010; 206:446–457.
17. Postberg F, et al. Discriminating contamination from particle components in spectra of Cassini's dust detector CDA. Planet Space Sci. 2009; 57:1359–1374.
18. Goldsworthy BJ, et al. Time of flight mass spectra of ions in plasmas produced by hypervelocity impacts of organic and mineralogical microparticles on a cosmic dust analyser. A&A. 2003; 409(3):1151–1167.
19. Srama R, Woiwode W, Postberg F, Armes SP, Fujii S, Dupin D, Ormond-Prout J, Sternovsky Z, Kempf S, Moragas-Klostermeyer G, Mocker A, et al. Mass Spectrometry of Hyper-Velocity impacts of organic micro grains. Rapid Commun Mass Spectrom. 2009; 23:3895–3906. [PubMed: 19924687]
20. Silverstein, RM., Webster, FX., Kiemle, DJ. Spectrometric Identification of Organic Compounds. Seventh Edition. A John Wiley and Sons, Inc.; New Jersey: 2005. p. 1-70.
21. Dass, C. Fundamentals of Contemporary Mass Spectrometry. First Edition. A John Wiley and Sons, Inc.; New Jersey: 2007. p. 210-238.
22. Schmidt J, Brilliantov N, Spahn F, Kempf S. Slow dust in Enceladus' plume from condensation and wall collisions in tiger stripe fractures. Nature. 2008; 451:685–688. [PubMed: 18256665]
23. Teolis BD, Perry ME, Magee BA, Westlake J, Waite JH. Detection and measurement of ice grains and gas distribution in the Enceladus plume by Cassini's Ion Neutral Mass Spectrometer. J Geophys Res. 2010; 115 A09222.
24. Yeoh SK, Chapman TA, Goldstein DB, Varghese P, Trafton LM. On understanding the physics of the Enceladus south polar plume via numerical simulation. Icarus. 2015; 253:205–222.
25. Matson DL, Castillo-Rogez JC, Davies AG, Johnson TV. Enceladus: A hypothesis for bringing both heat and chemicals to the surface. Icarus. 2012; 221:53–62.
26. de Leeuw G, et al. Production flux of sea spray aerosol. Reviews of Geophysics. 2011; 49(2)
27. Wilson TW, et al. A marine biogenic source of atmospheric ice-nucleation particles. Nature. 2015; 525:234–238. [PubMed: 26354482]
28. Leck C, Bigg EK. Comparison of sources and nature of the tropical aerosol with the summer high arctic aerosol. Tellus B. 2008; 60:118–126.
29. Gantt B, Meskhidze N. The physical and chemical characteristics of marine primary organic aerosol: a review. Atmos Chem Phys. 2013; 13:3979–3996.
30. Porco CC, Dones L, Mitchell C. Could it be snowing microbes on Enceladus? Assessing Conditions in its plume and implications for future missions. Astrobiology. 2017; 17:876–901. [PubMed: 28799795]
31. Srama R, et al. The Cassini cosmic dust analyzer. Space Sci Rev. 2004; 114:465–518.
32. Hillier JK, McBride N, Green SF, Kempf S, Srama R. Modelling CDA mass spectra. Planet Space Sci. 2006; 54:1007–1013. 38.

33. Postberg F, Kempf S, Srama R, Green SF, Hillier JK, McBride N, Grün E. Composition of jovian dust stream particles. Icarus. 2006; 183:122–134. 39.
34. Srama R, et al. The Cosmic Dust Analyzer onboard Cassini: ten years of discoveries. CEAS Space Jour. 2011; 2:3–16.
35. Fiege K, et al. Calibration of relative sensitivity factors for impact ionization detectors with high-velocity silicate microparticles. Icarus. 241:336–345.
36. Mocker A, et al. A 2 MV Van de Graaff accelerator as a tool for planetary and impact physics research. Rev Sci Instru. 2011; 82 095111-095111-8.
37. Delcorte A, Segda BG, Bertrand P. ToF-SIMS analyses of polystyrene and dibenzanthracene: evidence for fragmentation and metastable decay processes in molecular secondary ion emission. Surface Science. 1997; 381:18–32.
38. Stephan T, Jessberger EK, Heidd CH, Rost D. TOF-SIMS analysis of polycyclic aromatic hydrocarbons in Allan Hills 84001. MAPS. 2003; 38:109–116.
39. Wiederschein F, Vöhringer-Martinez E, Postberg F. Charge separation and isolation in strong water droplet impacts. Phys Chem. 2015; 17:6858–6864.
40. Le Roy L, et al. COSIMA calibration for the detection and characterization of the cometary solid organic matter. PSS. 2015; 105:1–25.
41. Waite JH Jr, et al. The Cassini Ion and Neutral Mass Spectrometer (INMS) investigation. Space Sci Rev. 2004; 114:113–231.
42. Perry ME, et al. Cassini INMS measurements of Enceladus plume density. Icarus. 2015; 257:139–162.
43. Kieffer SW, et al. A Clathrate Reservoir Hypothesis for Enceladus' South Polar Plume. Science. 2006; 314:1764–1766. [PubMed: 17170301]
44. Ingersoll AP, Pankine AA. Subsurface heat transfer on Enceladus: Conditions under which melting occurs. Icarus. 2010; 206:594–607.
45. Gaston CJ, et al. Unique ocean-derived particles serve as a proxy for changes in ocean chemistry. J Geophys Res. 2011; 116(D18)
46. Keene WC, et al. Chemical and physical characteristics of nascent aerosols produced by bursting bubbles at a model air-sea interface. J Geophys Res. 2007; 112 D21202.
47. Facchini MC, et al. Primary submicron marine aerosol dominated by insoluble organic colloids and aggregates. Geophys Res Lett. 2008; 35(17)
48. Russell LM, et al. Carbohydrate-like composition of submicron atmospheric particles and their production from ocean bubble bursting. PNAS. 2010; 107:6652–6657. [PubMed: 20080571]
49. Burrows SM, et al. A physically based framework for modeling the organic fractionation of sea spray aerosol from bubble film Langmuir equilibria. Atmos Chem Phys. 2014; 14:13601–13629.
50. Jayarathne T, et al. Enrichment of Saccharides and Divalent Cations in Sea Spray Aerosol During Two Phytoplankton Blooms. Environ Sci Technol. 2016; 50(21):11511–11520. [PubMed: 27709902]
51. Schmitt-Kopplin P, et al. Dissolved organic matter in sea spray: a transfer study from marine surface water to aerosols. Biogeosciences. 2012; 9:1571–1582.
52. McCollom TM, et al. The influence of carbon source on abiotic organic synthesis and carbon isotope fractionation under hydrothermal conditions. Geochim Cosmochim Acta. 2010; 74:2717–2740.
53. Milesi V, et al. Thermodynamic constraints on the formation of condensed carbon from serpentinization fluids. Geochim Cosmochim Acta. 2016; 189:391–403.
54. Williams LB, et al. Organic molecules formed in a “primordial womb”. Geology. 2005; 33:913–916.
55. Cody GD, et al. Establishing a molecular relationship between chondritic and cometary organic solids. Proc Natl Acad Sci USA. 2011; 108:19171–19176. [PubMed: 21464292]
56. Stevenson, FJ. Humus Chemistry: Genesis, composition, reactions. John Wiley and Sons Inc.; New York: 1982.
57. Hänninen KI, Klöcking R, Helbig B. Synthesis and characterization of humic acid-like polymers. The Science of the Total Environment. 1987; 62:201–210.

58. Alexander CMO'D, et al. The nature, origin and modification of insoluble organic matter in chondrites, the major source of Earth's C and N. Chem Erde. 2017; 77:227–256.
59. Alexander CMO'D, Fogel M, Yabuta H, Cody GD. The origin and evolution of chondrites recorded in the elemental and isotopic compositions of their macromolecular organic matter. Geochimica et Cosmochimica Acta. 2007; 71:4380–4403.
60. Derenne S, Robert F. Model of molecular structure of the insoluble organic matter isolated from Murchison meteorite. Meteoritics & Planetary Science. 2010; 45:1461–1475.
61. Remusat, L. Organic material in meteorites and the link to the origin of life. BIO Web of Conferences; 2014. 03001
62. Sephton M. Organic compounds in carbonaceous meteorites. Nat Prod Rep. 2002; 19:292–311. [PubMed: 12137279]
63. Pizzarello, S., Cooper, GW., Flynn, GJ. The nature and distribution of the organic material in carbonaceous chondrites and interplanetary dust particles. Meteorites and the Early Solar System II. Lauretta, D., McSween, HY., editors. University of Arizona Press; Tucson, AZ, USA: 2006. p. 625-651.
64. Bardyn A, et al. Carbon-rich dust in comet 67P/Churyumov-Gerasimenko measured by COSIMA/Rosetta. Mon Not R Astron Soc. 2017; 469:S712–S722.
65. Altwegg K, Balsiger H, et al. Organics in comet 67p – a first comparative analysis of mass spectra from rosina–dfms, cosac and ptolemy. Monthly Notices of the Royal Astronomical Society. 2017; 469:S130–S141.
66. Tissot, BP., Welte, DH. Petroleum Formation and Occurrence, Second Edition. Springer-Verlag; Berlin: 1984.
67. Didyk BM, Simoneit BRT. Hydrothermal oil of Guaymas Basin and implications for petroleum formation mechanisms. Nature. 1989; 342:65–69.
68. McKinnon, WB., et al. Composition, internal structure, and thermal evolution of Pluto and Charon. Pluto and Charon. Stern, SA., Tholen, DJ., editors. Univ. of Arizona Press; Tucson: 1997. p. 295-343.
69. Sephton MA, et al. Hydropyrolysis: A new technique for the analysis of macromolecular material in meteorites. Planet Space Sci. 2005; 53:1280–1286.
70. Kissel J, Krueger FR. The organic component in dust from comet Halley as measured by the PUMA mass spectrometer on board Vega 1. Nature. 1987; 326:755–760.
71. Schoell M. Multiple origins of methane in the Earth. Chem Geol. 1988; 71:1–10.
72. Von Damm KL, et al. The Escanaba Trough, Gorda Ridge hydrothermal system: Temporal stability and subseafloor complexity. Geochim Cosmochim Acta. 2005; 69:4971–4984.
73. Horányi M, Juhász A, Morfill GE. Large-sclae structure of Saturn's E-ring. Geophy Res Lett. 2008; 35 L04203.
74. Hsu, H-W., et al. Understanding the E-ring puzzle. AGU Fall General Assembly; 2016. Abstract P33E-01
75. Waite JH, et al. The process of Tholin formation in Titan's upper atmosphere. Science. 2007; 316:870–875. [PubMed: 17495166]
76. Lavvas P, et al. Aerosol growth in Titan's ionosphere. PNAS. 2013; 110:2729–2734. [PubMed: 23382231]
77. Charvat A, Abel B. How to make big molecules fly out of liquid water: applications, features and physics of laser assisted liquid phase dispersion mass spectrometery. Phys Chem Chem Phys. 2007; 9:3335–60. [PubMed: 17664960]
78. Klenner, F., et al. Analogue spectra for ice grain impacts onto the Cosmic Dust Analyser at different impact speeds. 2018. in preparation
79. Srama, R. Cassini-Huygens and Beyond – Tools for Dust Astronomy. Habilitation Thesis; University of Stuttgart: 2009.

Europe PMC Funders Author Manuscripts

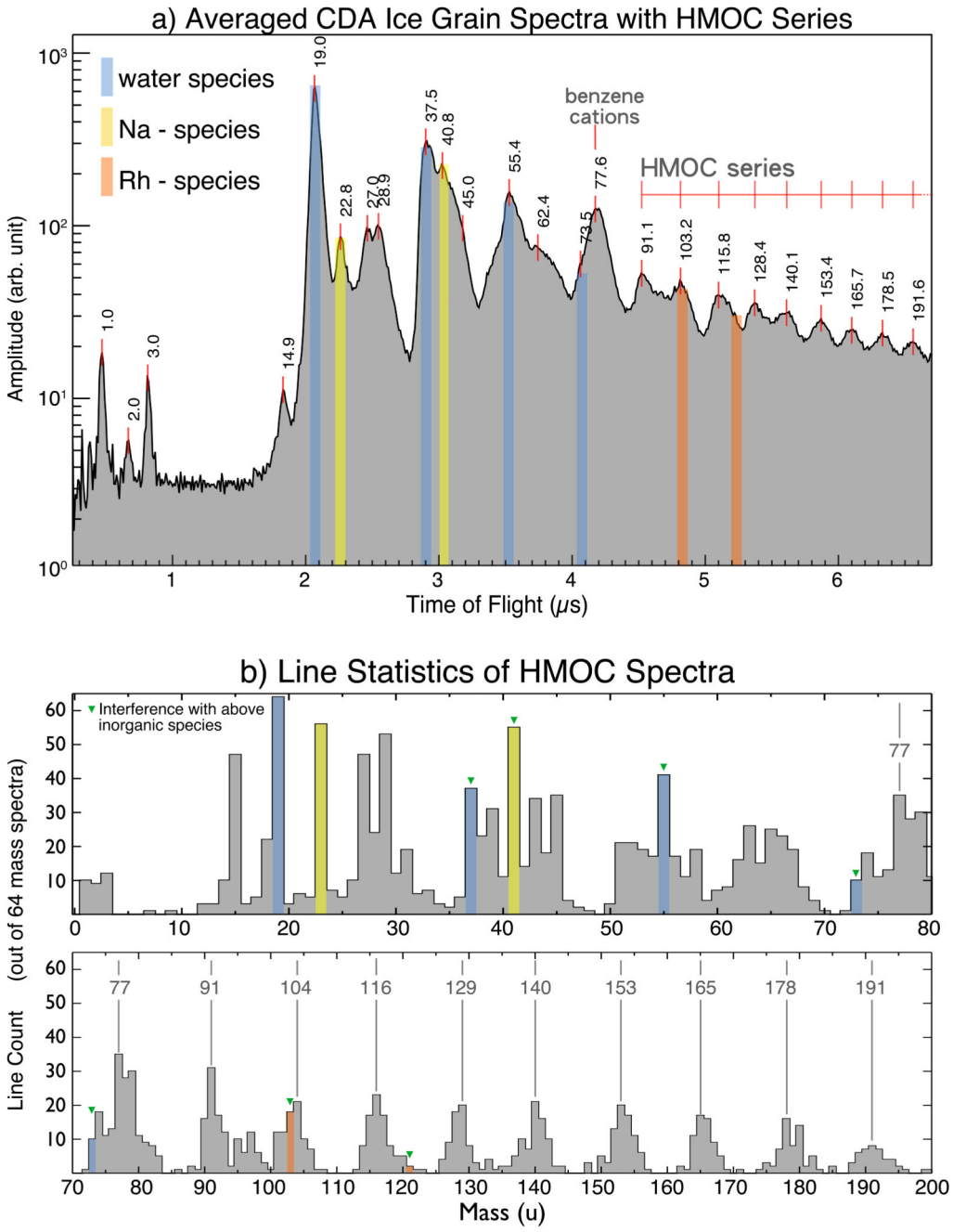

Figure 1. Co-added CDA HMOC spectrum and mass line histogram.

a) Time-of-flight spectrum representing the average of 64 high quality spectra (Methods 1d). The amplitudes of individual spectra were normalized and co-added. The corresponding masses of the peaks are labeled. The spectrum provides a representation of the average abundance of cation species. All signatures not color-shaded are exclusively or at least to a greater part due to organic cations as described in the text. Mass lines of exclusively inorganic origin are H_3O^+ at 19u and Na^+ at 23u. Mass lines where interference with inorganic cations is likely are: H_2O-H_3O^+ (37u), H_2O-Na^+ (41u), $(H_2O)_2$ -H_3O^+ (55u),

$(H_2O)_3$ -H_3O^+ (73u). CDA's target material rhodium and its water cluster forms cations at 103u and 121u (Rh^+, Rh-H_2O^+) that interfere with the HMOC pattern, but only in fast impacts (ED Fig. 3 for comparison of fast vs. slow impacts and ED Fig. 4 for examples of individual CDA spectra). For a semi-quantitative overview of spectral features in individual spectra in the data set see ED Fig. 1.

b) Occurrences ('counts') of resolved mass lines and 'flank peaks' in 64 high quality HMOC spectra (Methods 1d). In contrast to the spectrum shown in a) the histogram makes no distinction of the peak amplitude and just shows the frequency of occurrences of resolved mass lines. Above 80u the characteristic HMOC mass lines appear, preceded by the peaks from benzene-derived cations at 77u and 79u. A peak that can be identified around 95u in some spectra (Fig 1a) is in agreement with phenyl cations ($C_6H_5^+$, 77u) forming a water cluster (C_6H_5-H_2O^+), preferably at lower impact speeds (ED Figs. 1, 3). Organic mass lines below 45u show up preferentially at uneven masses, located at 15u, 27u, 29u, 39u, 41u, 43u (Fig. 1b) indicating the preference for uneven numbers of H atoms of typical cationic hydrocarbon fragmentation fingerprint (CH_3^+, $C_2H_3^+$, $C_2H_5^+$, $C_3H_3^+$, $C_3H_5^+$, $C_3H_7^+$). Other interpretations for each individual line are possible (e.g. HCN^+ (27u), COH^+ (29u), CH_3CO^+ (43u)) but the overall pattern suggests hydrocarbons or hydrocarbon fragments here. All signatures with possible major contributions from inorganic species are color-shaded as in a). The absolute masses in both panels have an intrinsic uncertainty of ±1u at 80u, and ±2u at 180u due to the limited calibration accuracy of CDA in this high-mass regime. The mass intervals between peaks, however, are accurate to the integer level.

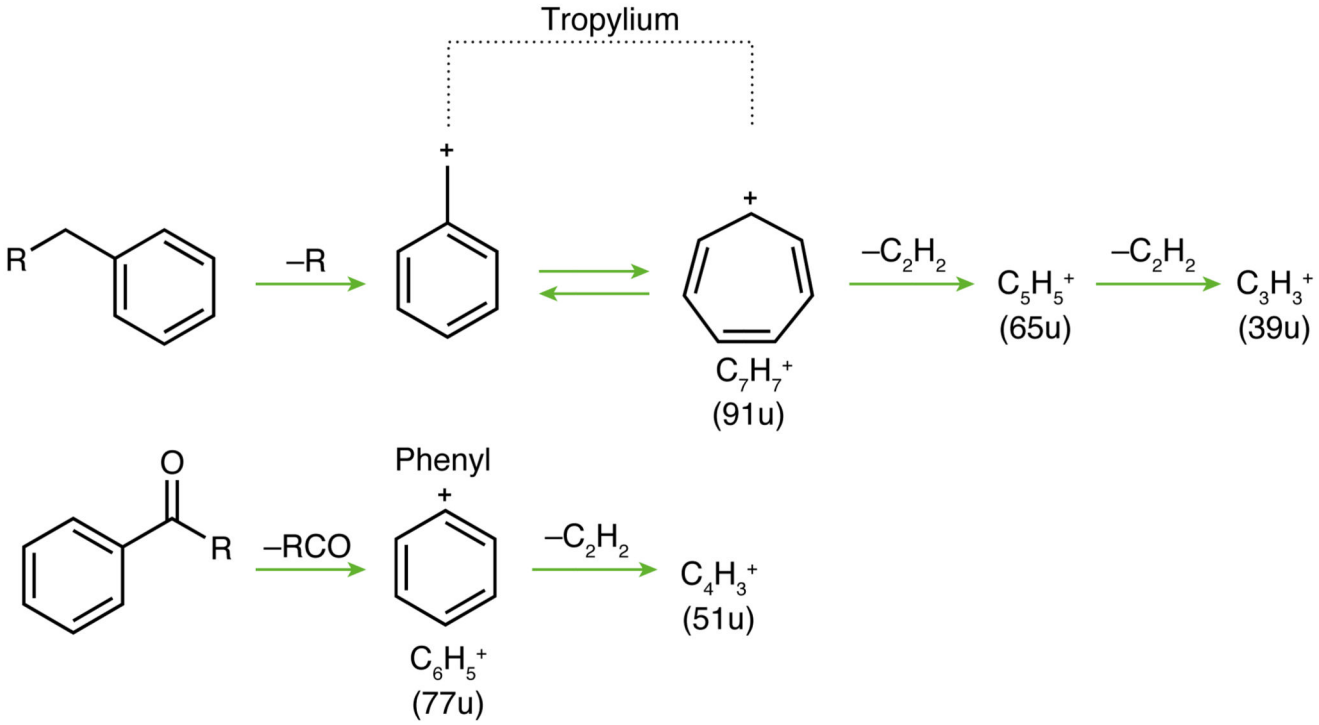

Figure 2. Formation of different aromatic cations

Although signatures in agreement with tropylium ions at ≈ 91u are present in every HMOC spectrum, they are on average about 3 times less abundant than the energetically favorable phenyl cation peak (1a). If, upon breakup, the molecular structure allowed for an integration of a C-H group (top) into the highly stable aromatic resonance structure of the tropylium ion (91u) the formation of phenyl cations (77u) would be suppressed (ED Fig. 2). Only if the macromolecular structure does not allow this (bottom), phenyl (77u) and benzenium cations (79u, not shown) are the preferred single-ringed cations (also ED Fig. 7). Note, fused benzene rings (like PAHs) do not form either of these abundant single-ringed species (Methods 2, ED Fig. 8). Subsequent losses of neutral acetylene (C_2H_2) from phenyl- and tropylium cations lead to smaller cationic fragments at 65u, 39u, and 51u, respectively[21] also seen in HMOC spectra (Fig. 1b).

Europe PMC Funders Author Manuscripts

Europe PMC Funders Author Manuscripts

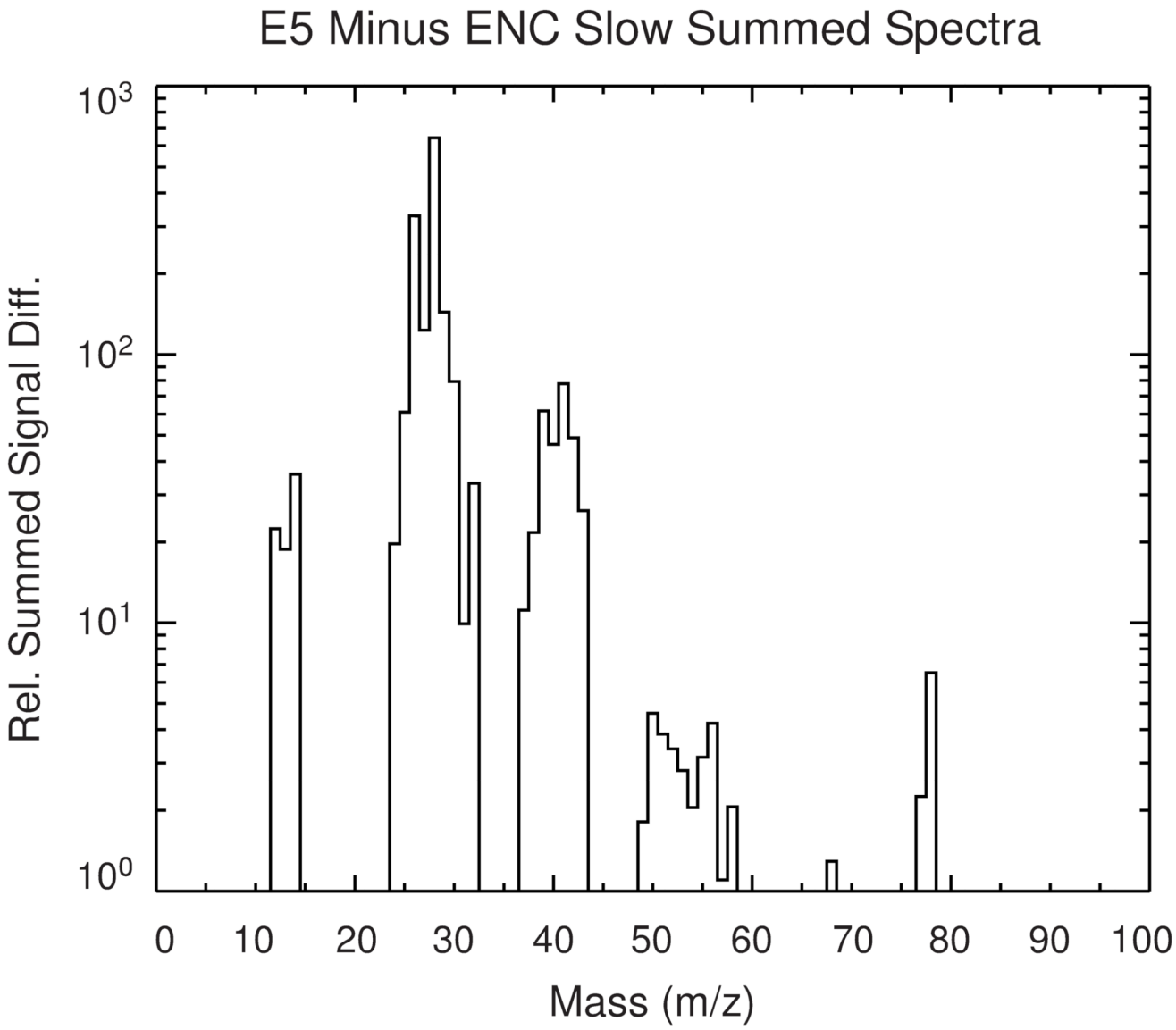

Figure 3. INMS organic fragmentation spectrum

By subtracting a plume-integrated INMS mass spectrum acquired at low velocities from a high velocity spectrum we obtain this residual we attribute to breakup products from high-mass species beyond the INMS mass limit at 99u (Methods 3a, ED Fig. 11). Abundances of these high-speed fragments are normalized to the abundance of CH_4 (via its CH_3^+ ion at 15u which therefore has no signal in the residual spectrum). The species at 77u and 78u match the CDA benzene-derived cations at 77u and 79u. In contrast to CDA, INMS measures the composition of the neutrals and thus the neutral benzene ring (78u) is expected to have the strongest signal here. Many of the more abundant low mass species are in agreement with aromatic fragmentation and oxygen-bearing parent molecules. Additional mass lines only seen at high-speed flybys (50 – 56u) and much elevated signals in other masses (37 – 42u and 25 – 28u) indicate unsaturated fragments $C_4H_{2\text{-}8}$, $C_3H_{1\text{-}6}$, $C_2H_{1\text{-}4}$, in agreement with aromatic breakup products. Aliphatic fragmentation is required for the high-mass end of the

C_2 and C_3 regions (29 – 30u and 43u). The overabundance at mass 28u (CO), 30u (likely H_2CO), and 31u (likely CH_3OH) requires a contribution of oxygen-bearing fragments (Methods 3a), consistent with CDA's observations.

Europe PMC Funders Author Manuscripts